

Article

Observation-constrained projections reveal longer-than-expected dry spells

<https://doi.org/10.1038/s41586-024-07887-y>

Received: 30 June 2023

Accepted: 29 July 2024

Published online: 18 September 2024

Open access

 Check for updates

Irina Y. Petrova¹✉, Diego G. Miralles¹✉, Florent Brient², Markus G. Donat^{3,4}, Seung-Ki Min^{5,6}, Yeon-Hee Kim⁵ & Margot Bador⁷

Climate models indicate that dry extremes will be exacerbated in many regions of the world^{1,2}. However, confidence in the magnitude and timing of these projected changes remains low^{3,4}, leaving societies largely unprepared^{5,6}. Here we show that constraining model projections with observations using a newly proposed emergent constraint (EC) reduces the uncertainty in predictions of a core drought indicator, the longest annual dry spell (LAD), by 10–26% globally. Our EC-corrected projections reveal that the increase in LAD will be 42–44% greater, on average, than ‘mid-range’ or ‘high-end’ future forcing scenarios currently indicate. These results imply that by the end of this century, the global mean land-only LAD could be 10 days longer than currently expected. Using two generations of climate models, we further uncover global regions for which historical LAD biases affect the magnitude of projected LAD increases, and we explore the role of land–atmosphere feedbacks therein. Our findings reveal regions with potentially higher- and earlier-than-expected drought risks for societies and ecosystems, and they point to possible mechanisms underlying the biases in the current generation of climate models.

Drought is one of the most devastating natural disasters of modern times⁷. Recent unprecedented drought events have demonstrated the high vulnerability and exposure of different societies and economic systems to this natural hazard⁶. The aggravated nature of present-day droughts, and their further expected exacerbation as a result of climate change, has drawn global attention to the accuracy of future projections and brought this topic to the forefront of governmental and public interests^{5,7}.

Despite the scientific consensus that the frequency and duration of dry extremes increase as a consequence of rising greenhouse gas (GHG) emissions in most regions of the world¹, uncertainty in future projections remains high, especially at regional scales^{3,4}. Moreover, the diversity of drought types and metrics complicates comparisons of existing studies⁸. Furthermore, model misrepresentation of the physical processes underlying rainfall deficits hampers accurate simulation of present-day drought characteristics^{9,10}, and leads to substantial differences between models in their response to GHG forcing on dry extremes⁴. The discrepancy between models in simulated historical precipitation intensity and frequency^{11,12} leads to inter-model differences in hydrological budgets¹³ and in the strength of relevant feedbacks, such as those involving soil moisture¹⁴ and clouds¹⁵. These systematic biases are known to contribute to divergence in model projections of dry extremes^{14,16–18}, while the role of internal variability or selected emissions scenario appears to be less relevant^{3,4,19}. Therefore, correcting for systematic precipitation errors is key to reducing the uncertainty in future drought projections²⁰, which is critical for the development of reliable and targeted adaptation strategies to minimize or even prevent future societal and environmental impacts²¹.

In this study, we revisit global drought projections for the twenty-first century and their uncertainty by exploring EC relationships in a metric of meteorological drought. The EC method has been established as a successful technique for reducing discrepancies in climate-model projections by identifying physically plausible relationships between past model errors and future prediction uncertainties²². Despite numerous ECs being proposed for a variety of hydro-climatic variables^{22,23}, constraints on drought characteristics have yet to be explored. To fill this gap, we focus on the simplest metric of meteorological drought, the LAD. This choice helps to avoid the uncertainties associated with more-complex drought metrics²⁴ and makes it easier to identify the physical mechanisms underlying the divergent trends in meteorological drought, reducing them to those most related to rainfall properties. Using past observational data of LAD and EC, we calibrate twenty-first-century LAD projections and reveal regions in which future LAD and the subsequent drought-associated risks to societies and ecosystems are potentially misrepresented in current climate-model projections.

Historical LAD and future projections

LAD is defined as the highest number of consecutive dry days per year and is calculated following the standardized definition by the Expert Team on Climate Change Detection and Indices (ETCCDI) (Methods). An observed historical (1998–2018) LAD climatology, based on seven satellite- and gauge-based products (Methods, Extended Data Fig. 1 and Supplementary Table 1), is shown in Fig. 1a. The global (50° S–50° N) patterns of observed LAD closely follow the main aridity gradients,

¹H-CEL, Ghent University, Ghent, Belgium. ²LMD/IPSL, Sorbonne Université, Paris, France. ³Barcelona Supercomputing Centre, Barcelona, Spain. ⁴Catalan Institution for Research and Advanced Studies (ICREA), Barcelona, Spain. ⁵Division of Environmental Science and Engineering, Pohang University of Science and Technology, Pohang, South Korea. ⁶Institute for Convergence Research and Education in Advanced Technology, Yonsei University, Incheon, South Korea. ⁷CECI, Université de Toulouse, CERFACS/CNRS, Toulouse, France. ✉e-mail: irina.petrova@ugent.be; diego.miralles@ugent.be

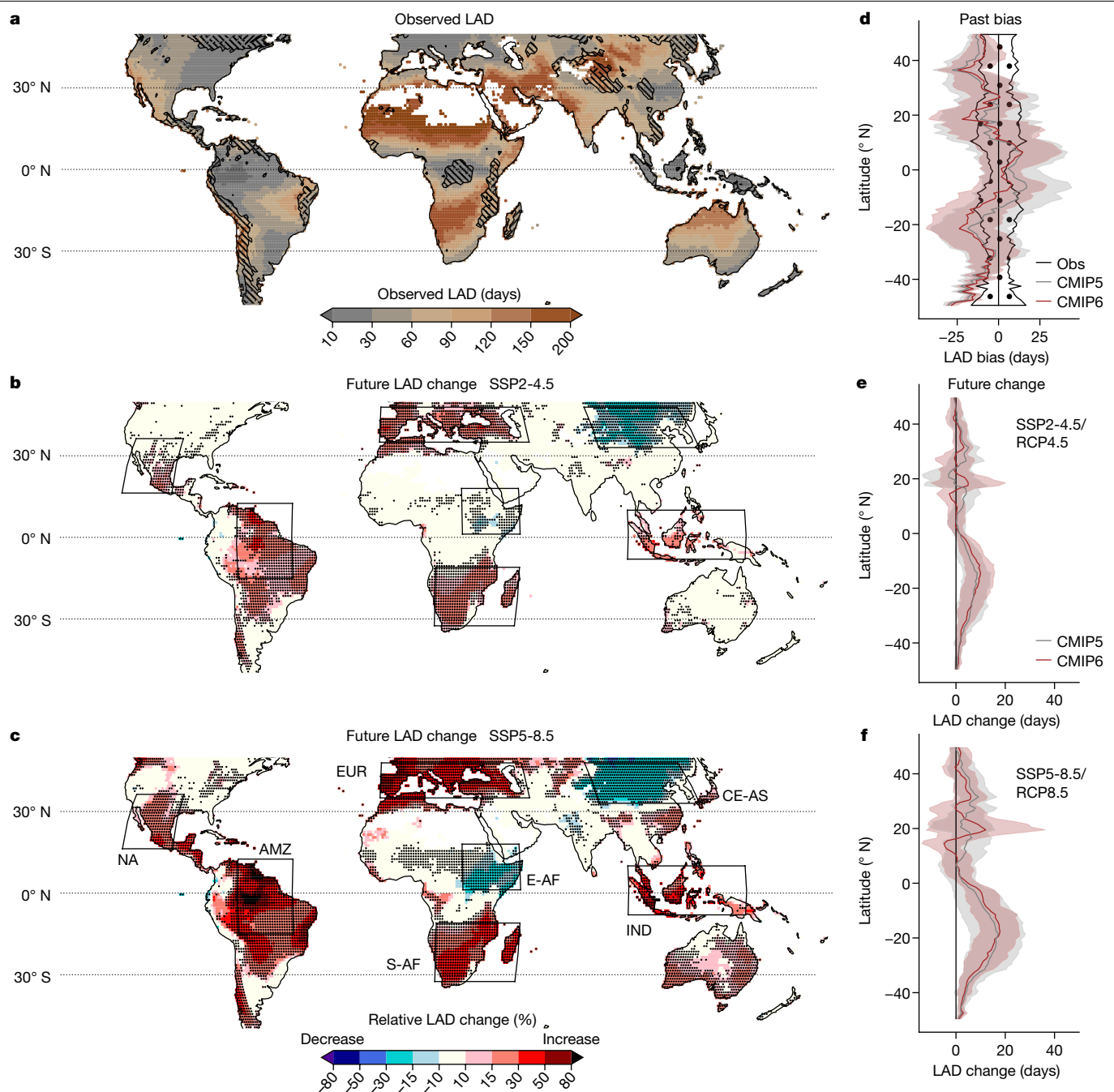


Fig. 1 | Observed LAD climatology and climate-model projections of future LAD change. **a**, Historical LAD climatology, averaged over seven observational datasets for the period 1998–2018. Hatched areas indicate regions with high uncertainty for which the observational standard deviation exceeds 30% of the observed climatological mean. **b,c**, Twenty-first-century relative LAD change (as a percentage of historical mean) as predicted by CMIP6 MEM under the SSP2-4.5 (**b**) and SSP5-8.5 (**c**) scenarios. Pixels where at least 70% of models agree on the sign of the change are marked with a dot. The rectangular boxes

highlight seven identified hotspot regions with the highest relative change (names are defined in the main text). **d**, Mean and s.d. of zonally averaged land-only historical LAD bias in the CMIP6 (red) and CMIP5 (grey) models relative to the observational median (black vertical line). The s.d. of the zonally averaged historical LAD among seven observational datasets is indicated (dotted area, **d**). **e,f**, Inter-model mean and s.d. of the magnitude of future LAD change under the SSP2-4.5/RCP4.5 (**e**) and SSP5-8.5/RCP8.5 (**f**) scenarios, where the vertical black line shows zero change.

ranging from only a few days in humid regions to more than 200 days in arid climates. At present, more than half of the global land area and about half of the world's population (that is, around 3.2 billion people for 2020) experience LAD periods of at least 2 months or longer on average (Extended Data Fig. 2).

According to the model ensemble mean (MEM) from the Climate Model Intercomparison Project phase 6 (CMIP6), about 50% of the global land surface will experience an increase in LAD of at least 5 days

by the end of the century under the ‘high-end’-emissions Shared Socio-economic Pathway (SSP) 5-8.5 scenario (Fig. 1c and Extended Data Fig. 3e). Although a global average increase of 5 days is expected, in some areas the increase could be up to 45 days. As Fig. 1b and Extended Data Fig. 3b show, following the more plausible²⁵ ‘mid-range’ emissions pathway not only reduces the increase in LAD to 2.4 days globally, and only 28 days at most locally, but it also lowers the percentage of areas that will have at least a 5-day increase from 50% to 30%. Both scenarios

Effect 1

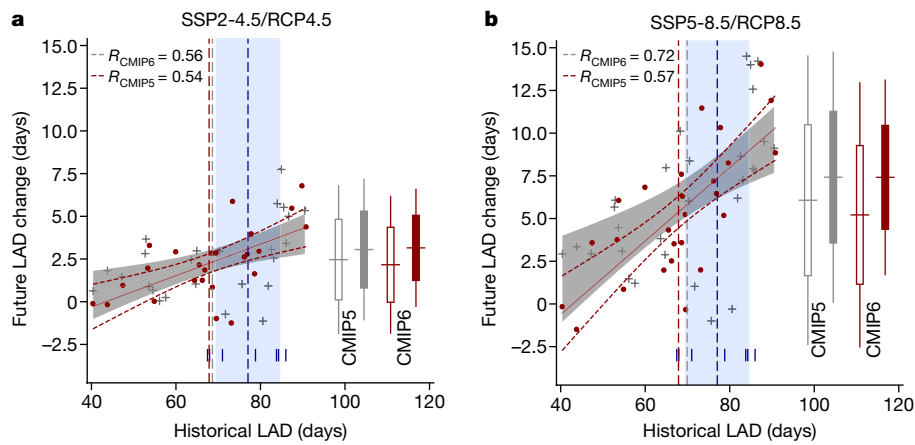


Fig. 2 | Emergent constraint on future LAD change. **a,b,** Inter-model relationship between historical LAD climatological mean and projected twenty-first-century LAD change from CMIP6 (red) and CMIP5 (grey) models under SSP2-4.5/RCP4.5 (**a**) and SSP5-8.5/RCP8.5 (**b**) scenarios. Every cross (CMIP5) and dot (CMIP6) represents the global (50° S–50° N) land average of a model. The corresponding MEMs are shown as vertical dashed lines.

The observational mean (blue line) and standard deviation (blue shading) are shown. The bars on the right of each graph show the mean, 66% and 90% value range of the future LAD change before (empty bars) and after (filled bars) EC correction for the CMIP5 and CMIP6 model ensembles. The specific models in each graph are defined in Extended Data Fig. 4c,d and Supplementary Tables 2 and 3.

reveal seven global hotspot regions where future LAD change will be the greatest relative to its present-day climatology (Fig. 1b,c); this includes regions of LAD increase, such as southwestern North America (NA), Amazonia (AMZ), Indonesia (IND), southern Africa and Madagascar (S-AF) and southern Europe (EUR), as well as regions where LAD is projected to decrease, such as Central–East Africa (E-AF) and Central–East Asia (CE-AS). In agreement with previous studies^{1,26}, we find that these hotspot regions remain at most unchanged from the previous (CMIP5) to the current (CMIP6) generation of climate models (Extended Data Fig. 3), and are also consistent with recent observational trends²⁷. Similarly, the inter-model uncertainty in simulated historical and future LAD remains consistently high in both CMIP5 and CMIP6 projections (Fig. 1d,e,f). The mean estimates of both model ensembles abidingly underestimate historical LAD climatology at subtropical latitudes and overestimate it in tropical regions, with the model uncertainty exceeding the observational spread by almost 100% in transitional zones (Fig. 1d). Future projections in both ensembles show some discrepancy in the sign of future LAD changes (mostly in the Northern Hemisphere) irrespective of the climate scenario (Fig. 1e,f) and show consistently high inter-model variability with standard deviations in projected LAD change reaching 1–2 months under the more-severe emissions scenario. The limited improvement from CMIP5 to CMIP6 in the inter-model uncertainty of meteorological drought projections and simulated precipitation characteristics has also been reported in recent studies^{19,28}.

Proposed emergent constraint

As clear evidence of the persistent inter-model discrepancy, Fig. 2 and Extended Data Fig. 4a,b show the model ensemble spread in future predicted global mean LAD (Extended Data Fig. 4a,b) and in the magnitude of its projected twenty-first-century change (Fig. 2) among 26 CMIP6 and 29 CMIP5 models (Methods and Supplementary Tables 2 and 3). As Extended Data Fig. 4a,b indicates, the variance in LAD projections does not notably decrease in the CMIP6 model ensemble compared with CMIP5. Moreover, under both emissions scenarios, future climatological LAD estimates are proportional to the historical LAD; models for which LAD values are higher than the historical MEM also predict a higher LAD by 2080–2100 (Extended Data Fig. 4a,b). The strong positive correlations between past and future LAD scatter (more than 0.98 for CMIP6 and more than 0.97 for CMIP5) indicate that historical model biases in LAD propagate linearly into

the future, which is consistent with previous assessments of future drought uncertainty^{3,4}. Furthermore, as Fig. 2 shows, the magnitude of the projected LAD increase also tends to be proportionally larger for models that overestimate LAD relative to the historical MEM. This emergent positive relationship across the model ensemble between the magnitude of the twenty-first-century LAD change and the historical LAD is supported by the significant ($P < 0.01$) inter-model correlations of 0.56 and 0.54 under the mid-range emissions scenario for the CMIP6 and CMIP5 ensembles, respectively (Fig. 2a). Under the more-severe emissions pathway, the correlations rise to 0.72 and 0.57 ($P < 0.01$) for the CMIP6 and CMIP5 ensembles, respectively, as the increase in LAD becomes higher for models that simulate longer historical LAD relative to its MEM (Fig. 2b). This finding indicates that the historical LAD biases in models may help to explain the magnitude of their LAD response to increases in GHG forcing. It also implies that there is a global ‘dry-model-gets-drier’ relationship in climate model projections.

As Fig. 2 demonstrates, the identified linear relationships are robust across the two climate-model ensembles, GHG emissions scenarios and time periods (Extended Data Fig. 5), with steeper slopes found for the more-severe scenario, as expected. Therefore, the relationship in Fig. 2 can serve as an EC and be used to correct future LAD projections (Methods). This assumption also requires the presence of a valid physical mechanism that can explain the obtained correlations²³. In our case, the physical processes underlying the emergent relationships are consistent with our understanding of differences in moist convection mechanisms and land–atmosphere feedbacks in models with ‘drier’ and ‘wetter’ climates and their response to global warming (see below). Including observational LAD estimates in the EC relation shows, first and foremost, that most climate models underestimate historical LAD (Fig. 2), which is consistent with previous findings^{29,30}, as well as with the general tendency by climate models to ‘rain too frequently and too light’³¹. Moreover, because it follows from the EC relationship, the same models that underestimate historical LAD are likely to project a smaller future LAD increase by the end of the twenty-first century. By calibrating each model projection against the observed LAD climatological value using the identified global EC, we find that the expected twenty-first-century LAD increase could be 42–44% greater on average than the CMIP6 MEM currently predicts for either GHG emissions scenario (Fig. 2, filled bars). This deviation, together with the pre-existing historical MEM bias, implies that the future global mean LAD could be on average 10 days longer than expected by 2080–2100.

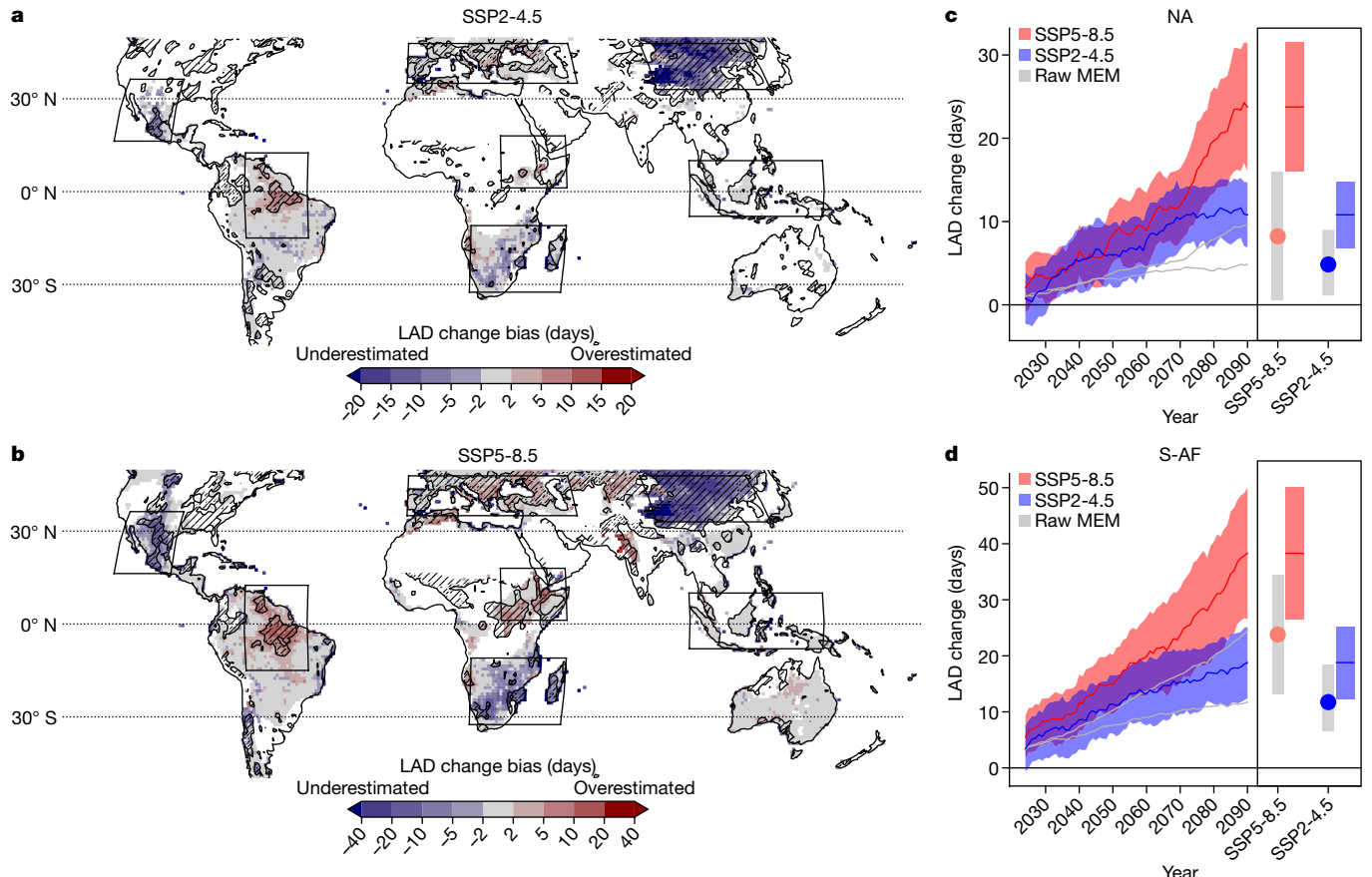


Fig. 3 | EC-corrected regional CMIP6 LAD projections. **a,b**, End of the twenty-first-century MEM bias of future LAD change projections for SSP2-4.5 (**a**) and SSP5-8.5 (**b**). Regions with small (less than 10%) twenty-first-century relative change or regions with invalid LAD data are shown as white (Methods). Regions with a significant local EC correlation ($R > 0.4$ and $P < 0.05$) are shown hatched. Hotspot regions are as indicated in Fig. 1. **c,d**, Time series of raw (grey)

and EC-corrected (coloured) annual projections of LAD change in two global hotspot regions for the two climate-change scenarios indicated. Time series are smoothed using 20-year running means. The bars on the right show end-of-century statistics. Uncertainty ranges of bars and time series represent the 66% range of model ensemble values for the end-of-century and annual statistics, respectively.

The EC calibration also narrows down the ensemble uncertainty of future projections by about 10% for SSP2-4.5 and by about 26% for SSP5-8.5, shifting its uncertainty range upwards, towards the higher values for LAD increases. Corrected CMIP5-based projections show a similar result to those based on CMIP6 (Fig. 2, grey bars). Taken together, the above findings indicate a potentially higher drought hazard to societies and ecosystems in coming decades than is predicted by current-generation climate models.

EC-corrected future LAD projections

Focusing on the recent CMIP6 model ensemble, we further demonstrate that the proposed EC on future LAD change remains valid ($R > 0.4$ and $P < 0.05$) at local scales for almost 30% of the global land surface for high-range, and 20% for mid-range, emissions scenarios (Extended Data Fig. 6). By calibrating each model projection against the observed LAD climatological value at the local scale (Methods), we obtain spatial insight into the regional biases in model-predicted LAD changes. As Fig. 3a,b shows, the local MEM bias in the magnitude of the future LAD change features a notable underestimation of the projected change in a number of hotspot regions.

Among the regions of projected LAD increase, the strongest underestimation, according to the EC, occurs in NA and S-AF drylands (Fig. 3a,b and Extended Data Fig. 8a,b). In these regions, the increase in LAD can be approximately twice as large as predicted by the uncorrected MEM irrespective of the emissions scenario, implying a higher drought risk in

these already water-scarce regions. This finding is strongly supported by the reported systematic overestimation of specific and relative humidity trends in models compared with observations, particularly in arid and semi-arid regions, resulting in a markedly slower drying trend for both land and atmosphere in models compared with observations³². The reconstructed time series of EC-corrected LAD change in these two regions shows that the originally projected end-of-century mean LAD increase under the SSP2-4.5 scenario of +5 days in NA may occur already by 2040, whereas in S-AF a drastic end-of-century increase of +12 days could be reached in the 2050s (Fig. 3c,d). Ultimately, Fig. 3c,d reveals that the EC-corrected LAD increase under the intermediate GHG SSP2-4.5 scenario closely resembles the uncorrected SSP5-8.5 forcing pathway in these regions. Taken together, these findings indicate an earlier-than-expected exposure to increased drought hazard and calls for a reassessment of the risks of (near-)future trends in these two regions.

Meanwhile, the tropical AMZ and E-AF reveal a potential overestimation of the model-projected LAD increase and decrease, respectively (Fig. 3a,b and Extended Data Fig. 8a,b). According to the EC, the future LAD increase in AMZ should be 4 days less than models project under SSP2-4.5, indicating even so a substantial increase of +7 days on average in the region after correction (Extended Data Fig. 8d). This finding aligns with the demonstrated tendency of climate models to overestimate future warming and drying in the Amazon³³. Conversely, an insignificant LAD decrease overestimation is found for E-AF (Extended Data Fig. 8g). Both regions, however, are well known

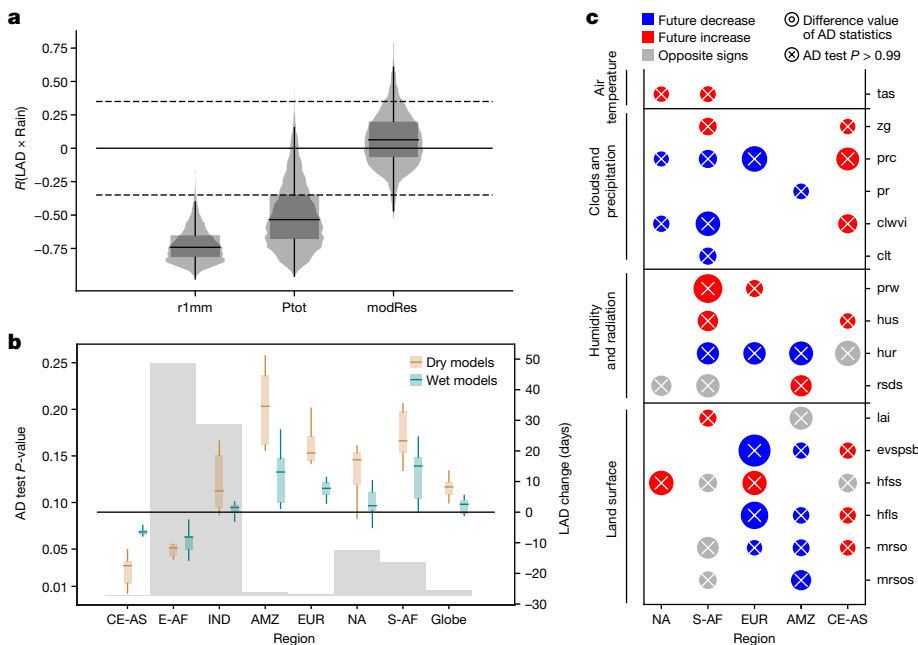


Fig. 4 | Link to physical mechanisms in CMIP6 models. **a**, Global statistics of inter-model correlation between historical LAD and annual number of wet periods (days with more than 1 mm of rain, r1mm), total annual rainfall (Ptot) and horizontal resolution of the model (modRes). Horizontal resolution at the Equator is estimated on the basis of longitude resolution of a corresponding atmospheric model. Violin plots show the probability density shape of correlations; box plots show the interquartile range (IQR, box) and $1.5 \times$ IQR (whiskers). **b**, Distribution of predicted future LAD changes in ‘dry’ (brown) and ‘wet’ (green) models in global hotspot regions and significance of the difference

between them (grey bars) according to the P -value of an Anderson–Darling (AD) test. Box plots show IQR and $1.5 \times$ IQR of LAD change in ‘dry’ or ‘wet’ models. **c**, Significant difference (P -value < 0.01) in projected future change in hydro-climatic variable between ‘dry’ and ‘wet’ models according to an Anderson–Darling test. Circle size indicates the magnitude of the difference (D -statistics) between two distributions in the Anderson–Darling test. The colour shows the sign of future variable change in ‘dry’ and ‘wet’ MEM. Variables are defined in Supplementary Table 4. Future changes for all variables were assessed for local dry periods (see Methods for details).

for being complex and notoriously difficult to simulate in terms of land–atmosphere interactions and future rainfall^{34–37}. Extended Data Fig. 8 confirms the very large LAD ensemble uncertainty in AMZ and E-AF; the lack of consensus in the sign of precipitation projections over E-AF in CMIP6 models is also seen in Extended Data Fig. 11. An overestimation of the future LAD increase found for parts of EUR (the Mediterranean and the Black Sea; Fig. 3a,b) is in agreement with earlier findings of overestimated future predicted drying for Europe^{14,18,38}. No significant difference is found in the IND hotspot region after the EC correction.

By contrast, a strong underestimation of the future LAD decrease is found for CE-AS (Fig. 3a,b and Extended Data Fig. 8a,b). According to the EC, the future LAD decrease there could be almost three times stronger than predicted by the MEM by 2100, and more than twice as strong by 2050, irrespective of the climate emissions scenario (Extended Data Fig. 8f). This could imply a 15-day reduction in LAD already by 2050 under the mid-range scenario. Whether the latter could lead to risks associated with more frequent rainfall and, as a result, a potentially higher- and earlier-than-expected risk of flooding in the highland arid regions of Asia^{39,40} merits further investigation. Although the region reveals the highest EC correlation across the globe (reaching 0.9 in places), it also has the largest observational uncertainty of the regions (Extended Data Fig. 1c) and is still one of the most complex regions for future precipitation and drought projections^{40–43}. All in all, the CE-AS domain stands out as the prominent global region for the ‘dry-model-gets-wetter’ relationship, and it seems to be decoupled from the rest of the global EC relationship (see Discussion). Validation tests on the sensitivity of future locally corrected LAD change to the choice of observational dataset showed overall robust future EC-corrected patterns, with some variations in the magnitude around topographically complex regions. These are the regions with the highest observational uncertainty (Extended Data Fig. 7).

Physical mechanisms underlying the EC

To explore possible physical mechanisms underlying this past–future LAD dependency, we focus on the SSP5-8.5-based results, because of their higher statistical significance in the EC relationship and LAD change, noting that similar (but milder) patterns are expected for the SSP2-4.5 scenario. Significant negative inter-model correlations of historical LAD climatology with the total number of wet days per year (-0.74) and the total annual rainfall (-0.51 ; Fig. 4a and Extended Data Fig. 9a,b) corroborate the link to a systematic error in climate models that is frequently referred to as ‘the drizzle problem’^{9,11,31}. The former correlation implies that models with shorter LAD tend to have more frequent and lighter rain, resulting in a greater number of wet days per year. The latter correlation indicates in turn that models with shorter LAD are also generally ‘wetter’, whereas models with longer LAD are ‘drier’. Contrary to this, the potential role of varying model resolution cannot be confirmed (Fig. 4a). This explicit separation of CMIP6 LAD ensemble into ‘drier’ and ‘wetter’ models is also likely to be reflected in the future climate response of models to GHG forcing^{14,16–18}. Consistent with earlier findings for Europe^{14,16} and the United States¹⁷, models that are identified as ‘dry’ in our study (Methods) project stronger responses to warming, and hence greater regional increases in LAD by 2080–2100, whereas ‘wet’ models project weaker responses and smaller regional increases (Fig. 4b). According to the Anderson–Darling test, the end-of-century LAD change distributions in the two model groups are found to be significantly different ($P < 0.05$) in all regions except IND and E-AF.

To gain a deeper understanding of the factors contributing to the divergent LAD response to increasing GHG forcing in regions with significant differences in Anderson–Darling test results, we examine variations in future changes of more hydro-climatic variables from the CMIP6 dataset. This analysis focuses specifically on locally

identified dry periods (see Methods), comparing the outcomes of ‘dry’ and ‘wet’ models (Methods and Supplementary Table 4). As Extended Data Fig. 11a shows, ‘dry’ models generally tend to simulate a stronger decrease, and ‘wet’ models a weaker decrease, in convective precipitation (prc) in regions where future LAD increase is projected. According to the Anderson–Darling test, the decrease in prc is found to be significantly different ($P < 0.01$) between ‘dry’ and ‘wet’ models for NA, S-AF and EUR, and is less significant ($P = 0.123$) for AMZ (Fig. 4c and Supplementary Table 5). Moreover, for EUR, inter-model historical LAD scatter correlates significantly with the projected change magnitude of prc, latent and sensible heat fluxes, relative humidity, cloud cover and temperature (Extended Data Fig. 10). Given the consistency of these dependencies, and the almost linear error propagation across the model ensemble, it can be assumed that the detected biases are not independent of one another, and that there are feedbacks between the predicted stronger reduction in prc and the larger decrease in relative humidity, cloudiness and latent heat flux, and the corresponding smaller increase in precipitable water and higher increase in sensible heat flux and temperature in ‘drier’ models for EUR (Extended Data Fig. 11a). This conclusion is consistent with the demonstrated role of land–atmosphere feedbacks in the divergence of future dryness and temperature projections in the CMIP5 ensemble for Europe^{14,38,44}.

Despite the visible discrepancies in identified key and correlated variables for the regions shown in Fig. 4c and Extended Data Fig. 10, feedbacks between changes in LAD, prc, atmospheric humidity, turbulent heat fluxes, shortwave radiation, temperature and cloud cover seem to be a plausible driver for the divergent future LAD change response in NA and AMZ, in agreement with the results for EUR. In NA, AMZ and EUR, ‘dry’ models consistently tend to simulate significantly larger increases in sensible heat flux, which is likely to be linked to larger increases in incoming short-wave radiation (Extended Data Fig. 11a). Both variables show significant differences in future changes between ‘dry’ and ‘wet’ models, according to the Anderson–Darling test (Supplementary Data Table 5). Larger increases in incoming shortwave radiation may be related to either a greater reduction in cloud cover and precipitable water (most notable in EUR and NA) or to a larger increase in temperature and hence a greater decrease in relative humidity and the condensed water path parameter (clearly differentiable in AMZ). These findings do not exclude a role for distinct key mechanisms in changes in future LAD trends for different regions, but overall they are in agreement with the differences in feedbacks and moist-convection scheme sensitivities inherent to ‘dry’ and ‘wet’ models that have been pointed out in previous studies^{14,38,45}. Likewise, the ‘drizzle problem’ in models has been shown to affect the radiation balance, because ‘wet’ models create more low-level clouds, which reduce incoming shortwave radiation⁴⁵. Moreover, ‘wet’ and ‘dry’ models have been shown to exhibit differences in the sensitivity of their moist-convection scheme to the dryness of the atmosphere, implying that ‘wet’ models simulate rain more easily because rain will start in a much drier atmosphere than it does for ‘dry’ models¹⁰. Amplified by global warming, the overall drier climate in ‘dry’ models will make it ever harder to reach this sensitivity threshold, and it will be reached less often¹⁰. All these mechanisms are consistent with our findings and with the identified ‘dry-model-gets-drier’ relationship in regions of future LAD increase.

Substantial discrepancies in the sign of the projected changes of some key hydro-climatic variables in the remaining domains (S-AF, E-AF and CE-AS) make it hard to link the identified dependencies to the relevant mechanisms in these regions (Fig. 4c). In S-AF, key variables such as soil moisture, sensible heat flux and incoming shortwave radiation show an opposite sign of change for ‘dry’ and ‘wet’ models (Fig. 4c and Extended Data Fig. 11a). In E-AF, prc, cloud cover, relative humidity, incoming shortwave radiation and leaf area index indicate a substantial spread in sign of future changes (Extended Data Fig. 11b). Similarly, large divergences in sign are found in the CE-AS domain for

relative humidity, soil moisture and sensible heat flux (Extended Data Fig. 11b). Although these apparent inconsistencies do not clarify the mechanisms underlying the LAD biases in these regions, they could guide further research aimed at addressing region-specific biases in climate and regional models.

Discussion

Our results show that climate model biases in the historical estimates of LAD are not only likely to persist into the future, but may be amplified by land–atmosphere feedbacks, significantly affecting the magnitude of the projected LAD change in at least 20–30% of global land areas. We find a consistent and significant ‘dry-model-gets-drier’ relationship across CMIP5 and CMIP6 model ensembles in five out of seven global hotspot regions, confirming that the same limitations of the underlying physical processes and uncertainties in relation to drought projection are likely to remain in the new generation of models. The analysis shows that errors in the parametrization of moist-convection processes leading to the ‘drizzle problem’³¹ is one of the plausible mechanisms that could explain the inter-model spread in historical and future LAD, and the identified ‘dry-model-gets-drier’ relation between them¹⁰. The question of whether convective-scheme limitations are a major driver of, or just one of the inter-dependent factors contributing to, systematic spread in models’ dryness projections remains open. Consistent with several regional studies^{14,16,38,46}, our results show that models with drier climates at present (models that simulate rain less frequently) tend to reinforce the drying and lack of rainfall initiation as the result of land–atmosphere feedbacks, namely more-vigorous increases in sensible heat flux and incoming shortwave radiation, and greater land and atmosphere warming. The role of land–atmosphere feedbacks in reinforcing drier climates in dry-biased models under increasing GHG forcing is not new³⁸, but our results clearly show that the same systematic errors remain in the latest generation of climate models, and thus emphasize the need to better represent these feedbacks and underlying physical processes to improve future drought projections. The results of inter-model correlation analyses to the hydro-climatic variables presented in this study point to problematic realms and dependencies in modelled processes on a regional scale, and thus may provide further guidance to the key mechanisms that must be addressed in models locally.

The mechanisms underlying the distinct ‘dry-model-gets-wetter’ dependency identified in the CE-AS and E-AF domains are hard to pinpoint. In the E-AF domain, there is no agreement across models on the sign of future changes in precipitation, probably because of the existing difficulty in simulating ‘long rain’ dynamics^{36,47}, whereas the CE-AS domain seems to be totally decoupled from the EC relationships identified for the rest of the world. Despite the strongest EC correlation ($R \approx 0.9$) in the domain, the ‘dry’–‘wet’ model ranking differs from that in other regions (Extended Data Fig. 9c–f). The latter might be linked to the much stronger role of dynamic than thermodynamic processes in regulating rainfall over CE-AS^{40,41} and the difficulty by models to capture these large-scale circulation shifts correctly^{42,43}. The stronger dependence of future LAD negative trends in the CE-AS region on the slower CO₂-adjustment mechanisms, such as uniform sea surface temperature warming, could also contribute to the difference in the EC relationship⁴⁸.

The validity of the EC-corrected LAD projections we propose in this study can be further scrutinized by revealing ECs for other types or stages of droughts and then finding an effective way to combine all predictors for a more-comprehensive assessment of future drought projections. Although the primary objective of this work was to identify valid EC relationships in the global dryness metric and refine its model projections around the multi-dataset observational mean, integrating the uncertainty of observational data into EC projections could offer in the future a more holistic insight into the total uncertainty of EC

estimates in regions. In such studies, the availability of a long observational time series would be crucial, as illustrated by our supplementary analysis (Extended Data Fig. 12e). Finally, reducing the still-large uncertainty of observational data should certainly be considered as a priority in regions such as CE-AS and E-AF (Extended Data Figs. 1 and 7) to adequately benchmark climate models⁴⁹.

In conclusion, our findings reveal extensive regions where climate change may cause stronger and earlier aggravation of drought-associated risks than previously expected under both the mid-range and high-end scenarios, and they emphasize the importance of reducing systematic climate-model errors, which are still largely caused by rainfall biases. Correcting these biases should be a priority and will increase the confidence of future projections of dry extremes, which is a prerequisite for effective reduction of drought risk in the near future, with direct benefits for human and natural systems.

Online content

Any methods, additional references, Nature Portfolio reporting summaries, source data, extended data, supplementary information, acknowledgements, peer review information; details of author contributions and competing interests; and statements of data and code availability are available at <https://doi.org/10.1038/s41586-024-07887-y>.

- Seneviratne, S. I. et al. Weather and climate extreme events in a changing climate. In *Climate Change 2021: The Physical Science Basis. Contribution of Working Group I to the Sixth Assessment Report of the Intergovernmental Panel on Climate Change* (eds Masson-Delmotte, V. et al.) 1513–1766 <https://doi.org/10.1017/9781009157896.013> (Cambridge Univ. Press, 2021).
- Almazroui, M. et al. Projected changes in climate extremes using CMIP6 simulations over SREX regions. *Earth Syst. Environ.* **5**, 481–497 (2021).
- Orlowsky, B. & Seneviratne, S. I. Elusive drought: uncertainty in observed trends and short- and long-term CMIP5 projections. *Hydrol. Earth Syst. Sci.* **17**, 1765–1781 (2013).
- Lu, J., Carbone, G. J. & Grego, J. M. Uncertainty and hotspots in 21st century projections of agricultural drought from CMIP5 models. *Sci. Rep.* **9**, 4922 (2019).
- Vatter, J., Wagnitz, P., Schmiester J. & Hernandez, E. *Drought Risk: The Global Thirst for Water in the Era of Climate Crisis* (WWF Germany, 2019).
- United Nations Office for Disaster Risk Reduction. *Special Report on Drought 2021* (United Nations, 2021).
- World Meteorological Organization. *State of the Global Climate 2021* https://library.wmo.int/doc_num.php?explnum_id=11178 (WMO, 2022).
- Yang, T., Ding, J., Liu, D., Wang, X. & Wang, T. Combined use of multiple drought indices for global assessment of dry gets drier and wet gets wetter paradigm. *J. Clim.* **32**, 737–748 (2019).
- Stephens, G. L. et al. Dreary state of precipitation in global models. *J. Geophys. Res. Atmos.* **115**, <https://doi.org/10.1029/2010JD014532> (2010).
- Bastin, S. et al. Impact of humidity biases on light precipitation occurrence: observations versus simulations. *Atmos. Chem. Phys.* **19**, 1471–1490 (2019).
- Sun, Y., Solomon, S., Dai, A. & Portmann, R. W. How often will it rain? *J. Clim.* **20**, 4801–4818 (2007).
- Nasrollahi, N. et al. How well do CMIP5 climate simulations replicate historical trends and patterns of meteorological droughts? *Water Resour. Res.* **51**, 2847–2864 (2015).
- Trenberth, K. E., Dai, A., Rasmusson, R. M. & Parsons, D. B. The changing character of precipitation. *Bull. Am. Meteorol. Soc.* **84**, 1205–1218 (2003).
- Vogel, M. M., Zscheischler, J. & Seneviratne, S. I. Varying soil moisture–atmosphere feedbacks explain divergent temperature extremes and precipitation projections in central Europe. *Earth Syst. Dyn.* **9**, 1107–1125 (2018).
- Hirota, N., Michibata, T., Shioigama, H., Ogura, T. & Suzuki, K. Impacts of precipitation modeling on cloud feedback in MIROC6. *Geophys. Res. Lett.* **49**, e2021GL096523 (2022).
- Orth, R., Zscheischler, J. & Seneviratne, S. I. Record dry summer in 2015 challenges precipitation projections in Central Europe. *Sci. Rep.* **6**, 28334 (2016).
- Herrera-Estrada, J. E., Satoh, Y. & Sheffield, J. Spatiotemporal dynamics of global drought. *Geophys. Res. Lett.* <https://doi.org/10.1002/2016GL071768> (2017).
- Topál, D., Hatvani, I. G. & Kern, Z. Refining projected multidecadal hydroclimate uncertainty in East-Central Europe using CMIP5 and single-model large ensemble simulations. *Theor. Appl. Climatol.* **142**, 1147–1167 (2020).
- Zhang, S. & Chen, J. Uncertainty in projection of climate extremes: a comparison of CMIP5 and CMIP6. *J. Meteorol. Res.* **35**, 646–662 (2021).
- Marraun, D. et al. Towards process-informed bias correction of climate change simulations. *Nat. Clim. Change* **7**, 764–773 (2017).
- Kreibich, H. et al. The challenge of unprecedented floods and droughts in risk management. *Nature* **608**, 80–86 (2022).
- Briant, F. Reducing uncertainties in climate projections with emergent constraints: concepts, examples and prospects. *Adv. Atmos. Sci.* **37**, 1–15 (2020).
- Hall, A., Cox, P., Huntingford, C. & Klein, S. Progressing emergent constraints on future climate change. *Nat. Clim. Change* **9**, 269–278 (2019).
- Taylor, I. H. et al. Contributions to uncertainty in projections of future drought under climate change scenarios. *Hydrol. Earth Syst. Sci. Discuss.* **9**, 12613–12653 (2012).
- Hausfather, Z. & Peters, G. P. Emissions – the ‘business as usual’ story is misleading. *Nature* **577**, 618–620 (2020).
- Ukkola, A. M., De Kauwe, M. G., Roderick, M. L., Abramowitz, G. & Pitman, A. J. Robust future changes in meteorological drought in CMIP6 projections despite uncertainty in precipitation. *Geophys. Res. Lett.* **47**, <https://doi.org/10.1029/2020GL087820> (2020).
- Wainwright, C. M., Allan, R. P. & Black, E. Consistent trends in dry spell length in recent observations and future projections. *Geophys. Res. Lett.* **49**, <https://doi.org/10.1029/2021GL097231> (2022).
- Li, J., Huo, R., Chen, H., Zhao, Y. & Zhao, T. Comparative assessment and future prediction using CMIP6 and CMIP5 for annual precipitation and extreme precipitation simulation. *Front. Earth Sci.* **9**, <https://doi.org/10.3389/feart.2021.687976> (2021).
- Kim, Y.-H., Min, S.-K., Zhang, X., Sillmann, J. & Sandstad, M. Evaluation of the CMIP6 multi-model ensemble for climate extreme indices. *Weather Clim. Extrem.* **29**, <https://doi.org/10.1016/j.wace.2020.100269> (2020).
- Funk, C. et al. Exploring trends in wet-season precipitation and drought indices in wet, humid and dry regions. *Environ. Res. Lett.* **14**, 115002 (2019).
- Chen, D., Dai, A. & Hall, A. The convective-to-total precipitation ratio and the “drizzling” bias in climate models. *J. Geophys. Res. Atmos.* **126**, <https://doi.org/10.1029/2020JD034198> (2021).
- Simpson, I. R. et al. Observed humidity trends in dry regions contradict climate models. *Proc. Natl Acad. Sci. USA* **121**, e2302480120 (2024).
- Cox, P. M. et al. Amazonian forest dieback under climate–carbon cycle projections for the 21st century. *Theor. Appl. Climatol.* **78**, 137–156 (2004).
- Monteverde, C., De Sales, F. & Jones, C. Evaluation of the CMIP6 performance in simulating precipitation in the Amazon river basin. *Climate* **10**, <https://doi.org/10.3390/cli0080122> (2022).
- Baker, J. C. A. et al. Robust Amazon precipitation projections in climate models that capture realistic land–atmosphere interactions. *Environ. Res. Lett.* **16**, 074002 (2021).
- Tierney, J. E., Ummenhofer, C. C. & deMenocal, P. B. Past and future rainfall in the Horn of Africa. *Sci. Adv.* **1**, e1500682 (2015).
- Baxter, A. J. et al. Reversed Holocene temperature–moisture relationship in the Horn of Africa. *Nature* **620**, 336–343 (2023).
- Selten, F. M., Bintanja, R., Vautard, R. & van den Hurk, B. J. J. M. Future continental summer warming constrained by the present-day seasonal cycle of surface hydrology. *Sci. Rep.* **10**, 4721 (2020).
- Hirabayashi, Y., Tanoue, M., Sasaki, O., Zhou, X. & Yamazaki, D. Global exposure to flooding from the new CMIP6 climate model projections. *Sci. Rep.* **11**, 3740 (2021).
- You, Q. et al. Recent frontiers of climate changes in East Asia at global warming of 1.5°C and 2°C. *NPJ Clim. Atmos. Sci.* **5**, 80 (2022).
- Wang, Z., Duan, A., Yang, S. & Ullah, K. Atmospheric moisture budget and its regulation on the variability of summer precipitation over the Tibetan Plateau. *J. Geophys. Res. Atmos.* **122**, 614–630 (2017).
- Dong, T. & Dong, W. Evaluation of extreme precipitation over Asia in CMIP6 models. *Clim. Dyn.* **57**, 1751–1769 (2021).
- Zhang, R., Chu, Q., Zuo, Z. & Qi, Y. Summertime moisture sources and transportation pathways for China and associated atmospheric circulation patterns. *Front. Earth Sci.* **9**, <https://doi.org/10.3389/feart.2021.756943> (2021).
- Donat, M. G., Pitman, A. J. & Angélil, O. Understanding and reducing future uncertainty in midlatitude daily heat extremes via land surface feedback constraints. *Geophys. Res. Lett.* **45**, 10,627–10,636 (2018).
- Terai, C., Caldwell, P. & Klein, S. Why do climate models drizzle too much and what impact does this have? In *AGU Fall Meeting Proceedings* <https://agu.confex.com/agu/fm16/meetingapp.cgi/Paper/162370> (2016).
- Herrera-Estrada, J. E. & Sheffield, J. Uncertainties in future projections of summer droughts and heat waves over the contiguous United States. *J. Clim.* **30**, 6225–6246 (2017).
- Wainwright, C. M. et al. ‘Eastern African paradox’ rainfall decline due to shorter but less intense long rains. *NPJ Clim. Atmos. Sci.* **2**, 34 (2019).
- Douville, H., Chadwick, R., Saint-Luc, M. & Medeiros, B. Drivers of dry day sensitivity to increased CO₂. *Geophys. Res. Lett.* **50**, <https://doi.org/10.1029/2023GL103200> (2023).
- Alexander, L. V. et al. Intercomparison of annual precipitation indices and extremes over global land areas from in situ, space-based and reanalysis products. *Environ. Res. Lett.* **15**, 055002 (2020).

Publisher’s note Springer Nature remains neutral with regard to jurisdictional claims in published maps and institutional affiliations.



Open Access This article is licensed under a Creative Commons Attribution-NonCommercial-NoDerivatives 4.0 International License, which permits any non-commercial use, sharing, distribution and reproduction in any medium or format, as long as you give appropriate credit to the original author(s) and the source, provide a link to the Creative Commons licence, and indicate if you modified the licensed material. You do not have permission under this licence to share adapted material derived from this article or parts of it. The images or other third party material in this article are included in the article’s Creative Commons licence, unless indicated otherwise in a credit line to the material. If material is not included in the article’s Creative Commons licence and your intended use is not permitted by statutory regulation or exceeds the permitted use, you will need to obtain permission directly from the copyright holder. To view a copy of this licence, visit <http://creativecommons.org/licenses/by-nc-nd/4.0/>.

© The Author(s) 2024

Methods

LAD measure definition

The LAD is calculated as the maximum annual number of consecutive dry days (CDD), following the definition of the Expert Team on Climate Change Detection and Indices (ETCCDI)⁵⁰. The LAD metric (CDD in ETCCDI tables) belongs to the core climate-extreme indices proposed by the ETCCDI⁵¹ and is routinely used in IPCC reports and by national drought monitors to assess concurrent and future changes in dryness, and to estimate the early risks associated with reduced water resources and heat extremes^{52,53}. A dry day is defined as a day with total rainfall below 1 mm; the 1 mm threshold is a commonly accepted limit to classify days as dry or wet, and it is routinely used in the global climate-extremes data sets, such as HadEX^{52,54,55}. The LAD calculation accounts for the possibility that dry spells can span across calendar years and assigns the value corresponding to the total LAD to the year in which the dry spell ends. Here, the historical LAD is not allowed to exceed 300 days to exclude hyper-arid regions. The historical LAD conditions are assessed for 1998–2018, which was selected as the common period of availability of seven observational datasets (see the next section). Future LAD climatology is evaluated from climate-model simulations over 2080–2100. The future change in LAD is assessed under different emissions scenarios as either an absolute or relative (normalized by historical mean) difference in LAD climatological means between the 2080–2100 and 1998–2018 periods.

Observational LAD data

Observational estimates of LAD values and their uncertainties across the globe are obtained from seven quasi-global (50° S– 50° N) daily-precipitation datasets (Supplementary Table 1). Six datasets are composed of three gauge-only and three gauge-corrected satellite products obtained from one of the largest consistent databases of daily-precipitation datasets, the Frequent Rainfall Observations on Grids (FROGS)⁵⁶. To calculate the LAD, FROGS precipitation data were post-processed using CLIMPACT software⁵⁷ developed at the University of New South Wales⁴⁹. One more independent LAD dataset is derived from a merged TRMM–CMORPH precipitation product using Python packages⁵⁸. The merging was done with the aim of filling gaps in TRMMv7 data by cumulative distribution function (CDF)-matching TRMMv7 (ref. 59) and CMORPHv0.1 (ref. 60) 3-hourly precipitation satellite products (Supplementary Table 1). All observation-based LAD fields were resampled to the common $1^{\circ} \times 1^{\circ}$ spatial resolution of FROGS.

The selection of the six LAD datasets from the extensive FROGS database for our analysis was based on their global and temporal coverage and further cross-validation analysis. Originally, we selected 11 FROGS products covering the entire spatio-temporal domain. However, 4 of the 11 products were not retained for further study because of inconsistent global coverage over time (SM2RAIN-CCI.1.DD), worse performance metrics in one of the twin datasets owing to a smaller number of gauges used (REGEN-LongTermStns) or worse performance metrics in a twin (with or without gauge correction) satellite-based dataset that had no gauge correction (GSMAP62-NRT-v6.0.1DD). Performance metrics here are referred to an averaged global mean inter-product Pearson correlation and global mean inter-product absolute difference (Extended Data Fig. 1a,b). Of the 11 FROGS-based products, CHIRP and CHIRPS showed the lowest inter-product correlations of LAD variability regardless of gauge correction (Extended Data Fig. 1a,b). Finally, it is crucial to emphasize that the application of an ensemble approach to observational data, as undertaken in the present study, is a necessary and valid solution to mitigate the inherent limitations associated with various observational products⁶¹.

LAD from CMIP6 and CMIP5 models

A total of 26 models from the 6th Coupled Model Intercomparison Project (CMIP6)⁶² were used to assess historical and future LAD estimates,

their uncertainties and the relationship between them (Supplementary Table 3). To do that, precipitation fields from the historical, moderate-end (SSP2-4.5) and high-end (SSP5-8.5) scenarios simulations were used to calculate LAD series using CLIMPACT software²⁹. To ensure the robustness of the investigated past–future model relationships, all analyses were repeated for 29 CMIP5 models⁶³ (Supplementary Table 2). For that, LAD estimates of CMIP5 data for the historical, RCP4.5 and RCP8.5 scenarios were obtained directly from the CLIMDEX database⁶⁴. To explore EC relationships in LAD model ensemble statistics, only the first realization from each model (r1) was used. Historical LAD conditions from CMIP6 models were considered for the period 1998–2014, according to the end year of their historical runs. Because historical simulations of CMIP5 models end in 2005, their present-day LAD climatology was calculated by combining the end of a historical run with the beginning of the RCP8.5 scenario, which has been common practice in previous studies⁶⁵. To account for the potential limitations of a shorter time span of historical data, further robustness tests were carried out over the full span of the available historical period up to 2100, that is, 1980–2100 for CMIP6 and 1860–2100 for CMIP5 (Extended Data Fig. 5a,b). The sensitivity of the global EC to the inclusion of the 1998–2018 period, which was characterized by strong La Niña conditions, was also tested and found to be non-significant (Extended Data Fig. 5c). All model data were rescaled to a common $1^{\circ} \times 1^{\circ}$ resolution using conservative first-order remapping interpolation of CDO⁶⁶. To account for the upscaling effect, the dependence of model biases on the original model resolution was tested and shown not to be relevant (Fig. 4a and Extended Data Fig. 12d). By comparing the daily rainfall-intensity distributions of historical LAD from both models and observations, we have also illustrated the robustness of the identified underestimation in the historical global model ensemble mean LAD in relation to the observed LAD around the specified threshold of 1 mm per day, that is, from less than 1 mm to at least 5 mm per day (Extended Data Fig. 12a–c).

Future LAD calibration using the EC approach

The EC technique is a well-established method of model validation that uses past observations to constrain future projections^{22,67,68}. First, it looks for a significant statistical relationship between a property of past climate, X , and a future climate, Y , across an ensemble of climate models; a credible physical mechanism must underlie the statistical relationship to reduce the probability of randomness in the revealed relationship and use it as an EC²³. In this study, variable X_i depicts the historical LAD climatology. Variable Y_i represents the magnitude of the twenty-first-century LAD change for the selected GHG emissions scenario, as estimated for each model (Fig. 2). A valid EC relationship between X_i and Y_i can then be described by a linear regression model:

$$Y_i = f(X_i) = a \times X_i + b \quad (1)$$

The strength and validity of the EC relationship $f(X_i)$ is assessed by the magnitude and the significance of the Spearman's rank correlation coefficient (R) calculated between X_i and Y_i series with the following criteria: a correlation coefficient of at least 0.4 with $P < 0.05$ (Extended Data Fig. 6c). Further, an actual 'observed' value of past X_i is substituted into equation (1) to derive the calibrated expectation and variance of future state Y_i (ref. 22). Thus, the future corrected LAD change expectation is obtained by projecting the mean observational LAD value on the y axis using the 'emergent' relationship $f(X_i)$. The calibrated variance of future LAD estimate is retrieved by projecting the observational mean on the uncertainty (prediction) interval of the regression line. The latter is assessed by a bootstrapping procedure. Although this approach does not fully account for the observational data uncertainty, it ensures consistency among the two model uncertainty estimates, that is, the uncertainty of a model sample at

Article

present and of its calibrated ensemble in the future. Observational uncertainty is still taken into account indirectly, because the EC relationship is assumed to be valid only if the observational uncertainty of X_i is small compared with the range of simulated X_i and Y_i values. In addition to the linear regression approach, the Kullback–Leibler (K–L) divergence method²² is tested, which allows the observational uncertainty to be taken into account. Applying this method to the longest observational REGEN-AllStation dataset showed consistent results for the EC-corrected global statistics (Extended Data Fig. 12e). Other important requirements of EC validity include: the presence and reproducibility of the relationship in other ensembles of models and over other time periods; and the proof of a physical mechanism that can explain the link between past and future variability across the models^{23,69}. Both conditions were tested and shown to hold for the ECs identified in this study, supporting their robustness. Credible mechanisms are explored and discussed in the manuscript, indicating that the uncovered EC relationships are not merely statistical. The results of a validation test that examines the sensitivity of the EC relationships to the time-period selection are shown in Extended Data Fig. 5.

In this study, the EC correction is applied to the global mean value of the LAD estimates, as well as locally (per grid cell), to explore the consistency of the revealed EC relationship over the globe and assess the spatial variation and regional dependence of biases in LAD model projections. The consistency of the local EC relationship across the globe is demonstrated in Extended Data Figs. 6 and 9c–f.

Linking EC to physical mechanisms

To understand which physical processes underlie the revealed EC relationship, CMIP6 historical and SSP5-8.5 scenario data for 16 hydro-climatic variables were downloaded from Google cloud storage⁷⁰ and processed using Pangeo software⁷¹. The 16 variables retrieved from various model realms at monthly scales are described in Supplementary Table 4. Historical and future temporal means of the variables are calculated for locally dry periods. These are identified using LAD data calculated from the TRMM–CMORPH precipitation dataset as the three climatological months where LAD periods typically end. The identified months of dry periods per region are: April–June for NA, June–August for AMZ, March–May for CE-AS, April–June for E-AF, July–September for S-AF, May–July for EUR, May–July for IND and the extended April–August for the global domain. In a next step, time series of each variable are retrieved for every domain separately for locally distinguished six ‘dry’ and six ‘wet’ models. Locally distinguished ‘dry’ models are those with historical LAD climatological values averaged per domain that are below the 25th percentile of the ensemble, or above the 75th for ‘wet’ models. Percentiles are assessed from the statistics of the climatological means of all models averaged over the selected domain. The retrieved data are averaged over historical (1990–2010) and future (2080–2100) periods for every ‘dry’ and ‘wet’ model. To increase the sample size for every model group, up to ten ensemble members (realizations r1–r10) are used for the Anderson–Darling test analysis (Fig. 4b,c) and in KDE plots (Extended Data Fig. 11), depending on data availability. Further validity criteria applied are: the spatial mask of the EC correlation being greater than 0.2; the presence of at least four available ‘dry’ and ‘wet’ models for the Anderson–Darling test; and at least six available models for the correlation analysis.

Data availability

All input data sources used in this study are referenced in the Methods. Precipitation satellite products are publicly available from the FROGS database (<https://frogs.ipsl.fr/>). The raw CMIP5 LAD data used in this study are available from CLIMDEX database (<https://climate-modelling-canada.ca/climateuserdata/climdex/>). Raw CMIP6 LAD data are

available by request from the corresponding authors. The output data sets produced in this study and required for reproducing the main figures of the paper are available at <https://doi.org/10.5281/zenodo.11636527> (ref. 72). The Python software used for data plotting and processing is available at <https://www.python.org/>.

Code availability

The code for the emergent constraint calculation and analysis is available at <https://doi.org/10.5281/zenodo.10886174> (ref. 73). The codes required for reproducing the main figures of this study are available at <https://doi.org/10.5281/zenodo.11637360> (ref. 74).

50. Zhang, X. et al. Indices for monitoring changes in extremes based on daily temperature and precipitation data. *Wiley Interdiscip. Rev. Clim. Change* **2**, 851–870 (2011).
51. Zhang, X. ETCCDI climate change indices. <https://etccdi.pacificclimate.org/> (2020).
52. Donat, M. G. et al. Updated analyses of temperature and precipitation extreme indices since the beginning of the twentieth century: the HadEX2 dataset. *J. Geophys. Res. Atmos.* <https://doi.org/10.1002/jgrd.50150> (2013).
53. Field, C. B. et al. (eds) *Managing the Risks of Extreme Events and Disasters to Advance Climate Change Adaptation* (Cambridge Univ. Press, 2012).
54. Alexander, L. V. et al. Global observed changes in daily climate extremes of temperature and precipitation. *J. Geophys. Res. Atmos.* **111**, <https://doi.org/10.1029/2005JD006290> (2006).
55. Dunn, R. J. H. et al. Development of an updated global land in situ-based data set of temperature and precipitation extremes: HadEX3. *J. Geophys. Res. Atmos.* **125**, <https://doi.org/10.1029/2019JD032263> (2020).
56. Roca, R. et al. FROGS: A daily $1^\circ \times 1^\circ$ gridded precipitation database of rain gauge, satellite and reanalysis products. *Earth Syst. Sci. Data* **11**, 1017–1035 (2019).
57. Climpact <https://climpact-sci.org/> (2012).
58. Python Language Reference, v.3.7 <https://www.python.org> (2019).
59. Huffman, G. J. et al. The TRMM multisatellite precipitation analysis (TMPA): quasi-global, multiyear, combined-sensor precipitation estimates at fine scales. *J. Hydrometeorol.* **8**, 38–55 (2007).
60. Xie, P. et al. Reprocessed, bias-corrected CMORPH global high-resolution precipitation estimates from 1998. *J. Hydrometeorol.* **18**, 1617–1641 (2017).
61. Bador, M. et al. Impact of higher spatial atmospheric resolution on precipitation extremes over land in global climate models. *J. Geophys. Res. Atmos.* **125**, <https://doi.org/10.1029/2019JD032184> (2020).
62. Eyring, V. et al. Overview of the Coupled Model Intercomparison Project Phase 6 (CMIP6) experimental design and organization. *Geosci. Model Dev.* **9**, 1937–1958 (2016).
63. Taylor, K. E., Stouffer, R. J. & Meehl, G. A. An overview of CMIP5 and the experiment design. *Bull. Am. Meteorol. Soc.* **93**, 485–498 (2012).
64. Sillmann, J. ETCCDI extremes indices archive. <https://climate-modelling.canada.ca/climateuserdata/climdex/index.shtml>.
65. Donat, M. G., Angélil, O. & Ukkola, A. M. Intensification of precipitation extremes in the world's humid and water-limited regions. *Environ. Res. Lett.* <https://doi.org/10.1088/1748-9326/ab1c8e> (2019).
66. Schulzweida, U. CDO User Guide (2.1.0). Zenodo <https://doi.org/10.5281/zenodo.7112925> (2022).
67. Collins, M. et al. Quantifying future climate change. *Nat. Clim. Change* **2**, 403–409 (2012).
68. Eyring, V. et al. Taking climate model evaluation to the next level. *Nat. Clim. Chang.* **9**, 102–110 (2019).
69. Caldwell, P. M. et al. Statistical significance of climate sensitivity predictors obtained by data mining. *Geophys. Res. Lett.* **41**, 1803–1808 (2014).
70. CMIP6 data from WCRP. Google Cloud Catalogue. <https://cloud.google.com/datasets>.
71. Pangeo Team. PANGEO: A community platform for Big Data geoscience. <https://pangeo.io/> (2018).
72. Petrova, I. Y. Observation-constrained projections reveal longer-than-expected dry spells. Source data. Zenodo <https://doi.org/10.5281/zenodo.11636527> (2024).
73. Brent, F. Reducing uncertainties in climate projections with emergent constraints: concepts. Source code: emergent constraints. Zenodo <https://doi.org/10.5281/zenodo.10886174> (2024).
74. Petrova, I. Y. Observation-constrained projections reveal longer-than-expected dry spells. Source code. Zenodo <https://doi.org/10.5281/zenodo.11637360> (2024).
75. Socioeconomic Data and Applications Center. Gridded Population of the World (GPW), v4. <https://sedac.ciesin.columbia.edu/data/collection/gpw-v4> (1995).

Acknowledgements I.Y.P. acknowledges support from the BOF research fund of Ghent University (BOF20/PDO/057). D.G.M. acknowledges support from the European Research Council (HEAT, 101088405). S.-K.M. acknowledges a National Research Foundation of Korea grant from the Korean government (NRF2021R1A2C300736). F.B. acknowledges funding from grant MOBYDYC (ANR-22-CE01-0005). M.G.D. is grateful for funding from the Horizon 2020 LANDMARC project (grant agreement no. 869367) and the Horizon Europe EXPECT project (grant no. 101137656). I.Y.P. thanks the Pangeo project for free access to the data catalogue and tools of the Pangeo platform. The computing resources and services used were provided by the VSC (Flemish Supercomputer Center), funded by the Research Foundation – Flanders (FWO) and the Flemish government.

Author contributions I.Y.P. and D.G.M. conceived the study and designed the research; I.Y.P. did the research, carried out the calculations, prepared the figures and wrote the paper with input from D.G.M.; F.B. developed and provided the emergent constraint code; S.-K.M. and Y.-H.K. provided CMIP-based LAD (CDD) and rain data; M.B. provided LAD (CDD) data from FROGS; and all authors revised the manuscript and provided feedback.

Competing interests The authors declare no competing interests.

Additional information

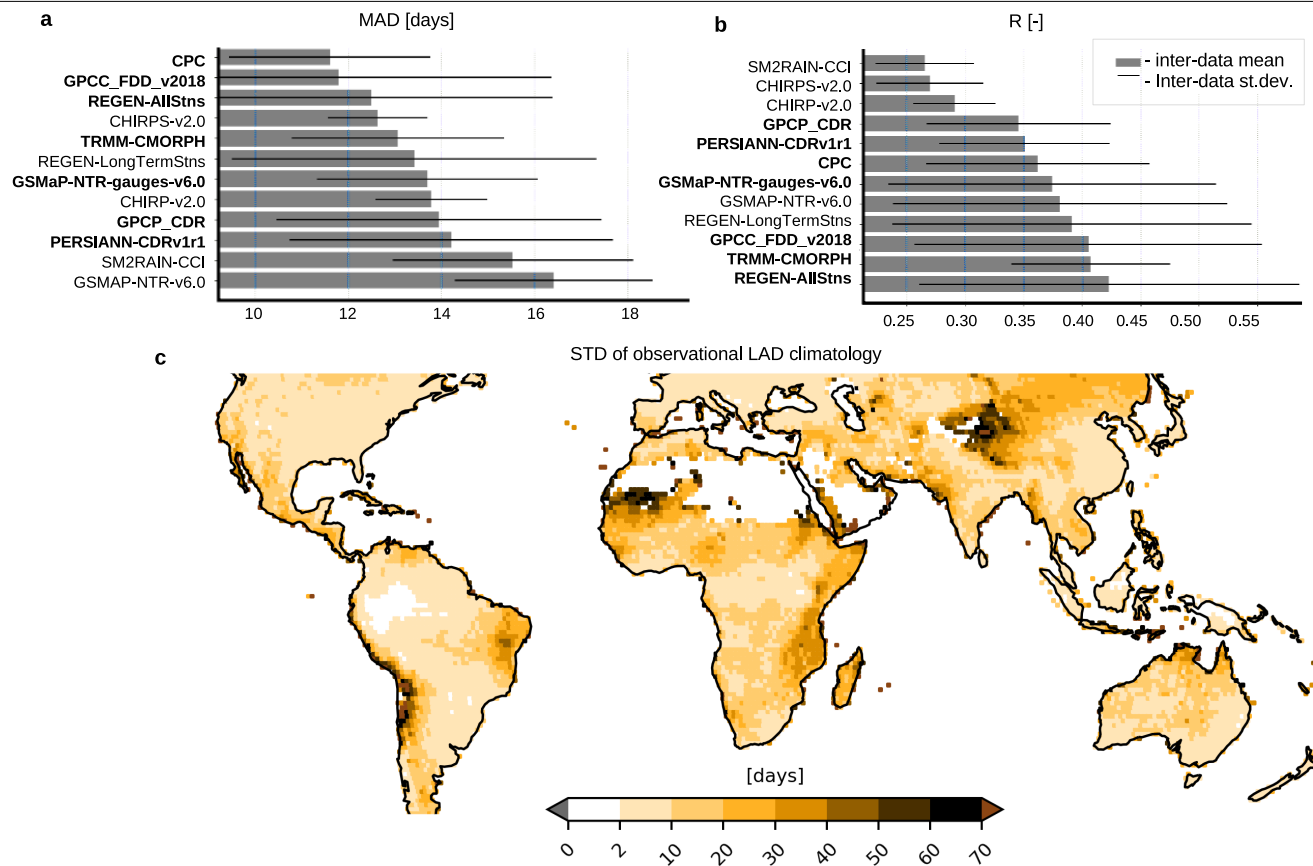
Supplementary information The online version contains supplementary material available at <https://doi.org/10.1038/s41586-024-07887-y>.

Correspondence and requests for materials should be addressed to Irina Y. Petrova or Diego G. Miralles.

Peer review information *Nature* thanks Richard Allan and the other, anonymous, reviewer(s) for their contribution to the peer review of this work.

Reprints and permissions information is available at <http://www.nature.com/reprints>.

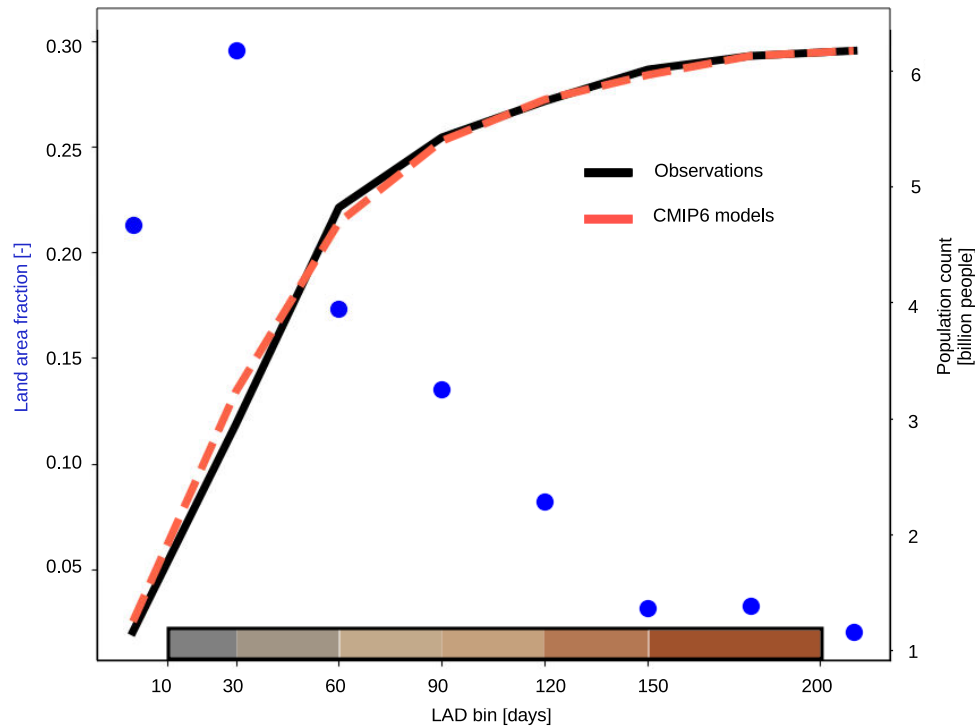
Article



Extended Data Fig. 1 | Uncertainty of observational LAD estimates.

a, b, Global mean and standard deviation of inter-product mean absolute difference (MAD) (a) and Pearson correlation (R) (b) among 12 precipitation data sets: 11 pre-selected FROGS data sets⁵⁶ and an independent merged TRMM–CMORPH product (see Methods and Table S1). Prior to constructing

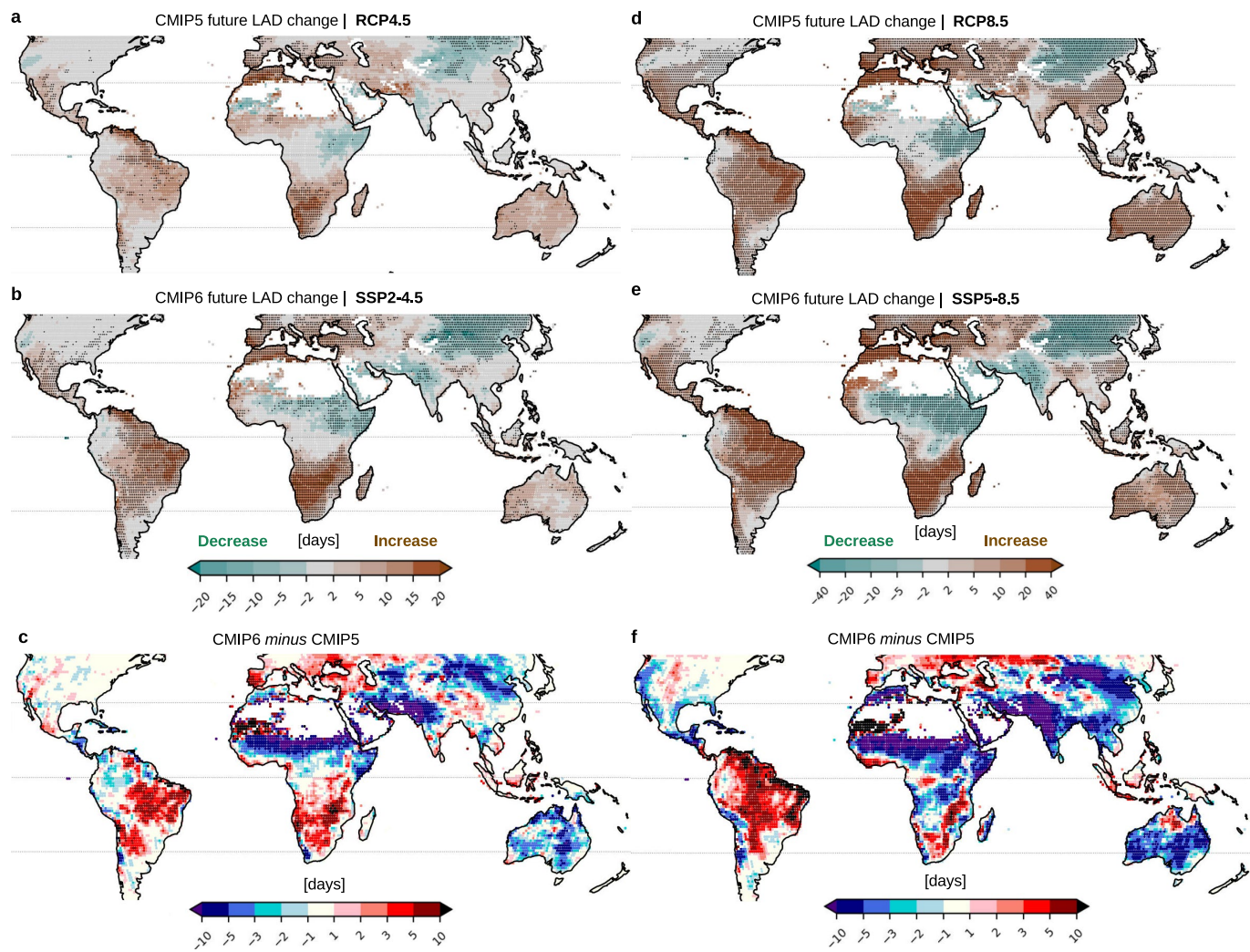
bar plots, MAD and R obtained per dataset are averaged over the global land (50°S – 50°N). The 7 products which are finally selected based on MAD, R and dataset characteristics (see Methods) for further study are highlighted. **c**, Local standard deviation of LAD of the 7 selected precipitation products.



Extended Data Fig. 2 | Characteristics of global LAD distribution. Global land area fraction corresponding to a particular LAD climatological value range (blue dots). Cumulative population count over the same LAD range bins,

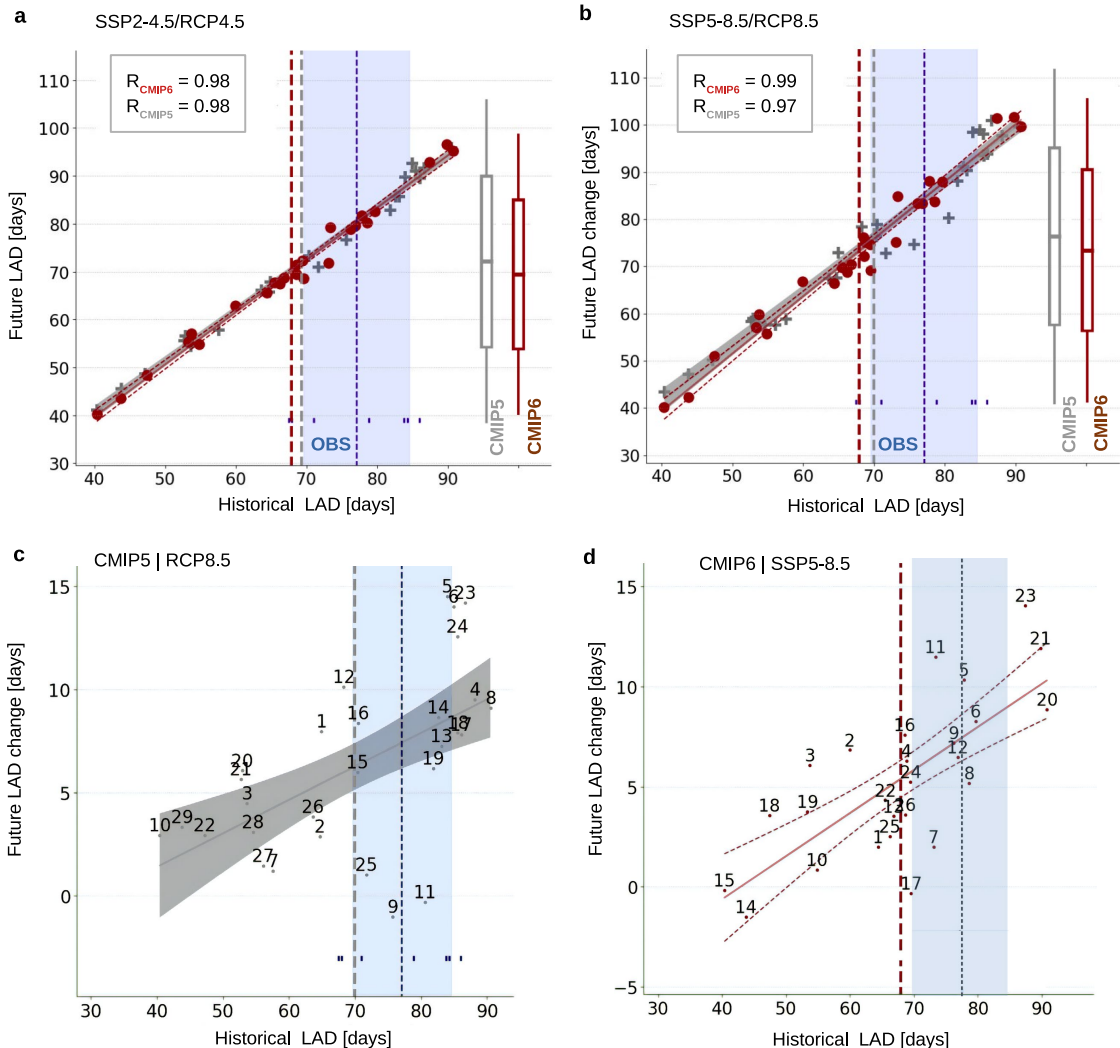
calculated from either observational (black) or CMIP6 model mean (red), is shown as lines. Colour code of LAD bins corresponds to the colour bar in Fig. 1a. Population data are extracted from GPW-v4⁷⁵ for the year 2020.

Article



Extended Data Fig. 3 | Future LAD change. **a,b,d,e** 21st century change in LAD predicted by CMIP6 (b,e) and CMIP5 (a,d) MEM under SSP5-8.5 (RCP8.5) and SSP2-4.5 (RCP4.5) scenarios. Pixels where at least 70% of models agree on the

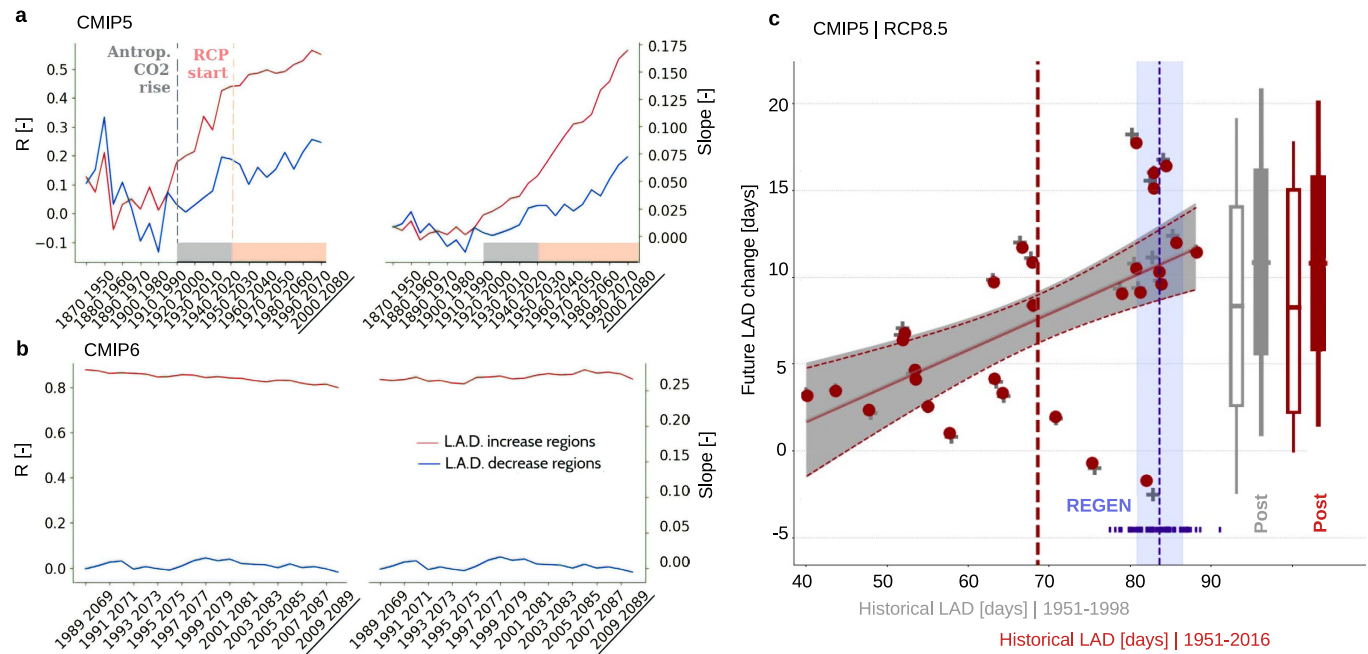
sign of the change are marked with a dot. **c,f** Difference in the future LAD change between CMIP6 and CMIP5 ensemble means under the SSP2-4.5 (RCP4.5) (c) and SSP5-8.5 (RCP8.5) (f) scenarios.



Extended Data Fig. 4 | Linear past-future LAD relationship. **a,b**, Correlation between historical and future LAD climatology in CMIP5 and CMIP6 ensembles for the ‘mid-range’ (**a**) and ‘high-end’ (**b**) emission scenarios; bar plots show mean, 66% and 90% range of future LAD statistics. **c,d**, EC relationship between historical LAD climatology and its 21st century change under the ‘high-end’

emission pathway scenario in CMIP5 (**c**) and CMIP6 (**d**) models. Every dot (CMIP6) and cross (CMIP5) represent the global land average of a model. Corresponding MEMs are shown as vertical dashed lines. Observational mean and uncertainty, 1 standard deviation (blue shading), is given. Model names corresponding to the numbers are given in Tables S2–S3.

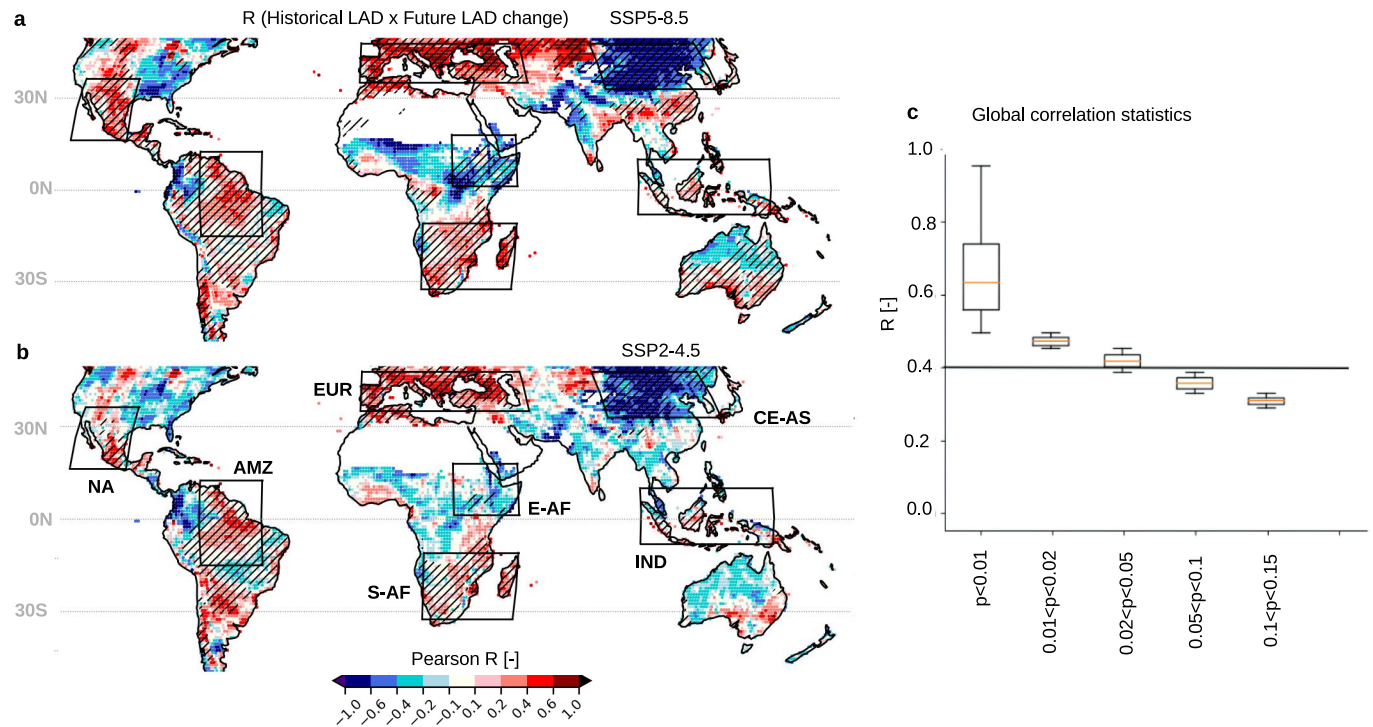
Article



Extended Data Fig. 5 | EC relationship sensitivity to the time period.

a,b, Inter-model Spearman rank correlation coefficient (R) and slope of the regression line between historical LAD and its future change (+80 years from the historical) for CMIP5 (**a**) and CMIP6 (**b**) models. The regions are split to future LAD increase (red line) and LAD decrease (blue line) regions. The time series represent 20-year moving averages. Different starting dates for CMIP5 and CMIP6 are defined by data availability. **c**, CMIP5-based EC relationship

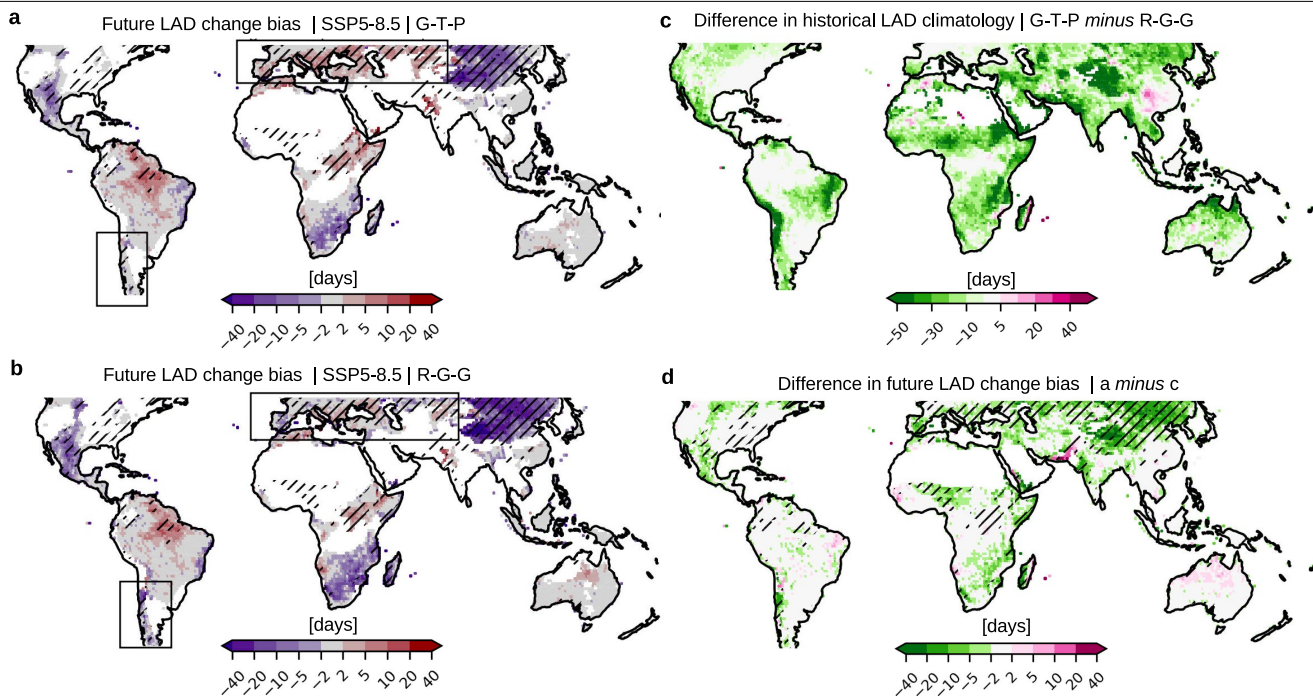
assessed for two different historical periods of 1951–1998 (grey) and 1951–2016 (red). Here, REGEN dataset is selected as the observational dataset with the longest time-period. Every dot/cross represents the global land average of a model. Corresponding MEMs are shown as vertical dashed lines. Observational mean and uncertainty, 1 standard deviation (blue shading), is given. Bars show a mean, 66 and 90% value range of the future LAD prior (empty bar) and post (filled bar) EC correction.



Extended Data Fig. 6 | Global EC strength and consistency. **a,b**, Inter-model correlation between historical LAD in CMIP6 model ensemble and its corresponding magnitude of the 21st century change for **(a)** SSP5-8.5 and **(b)** SSP2-4.5 emission scenarios. Correlations higher than 0.4 ($p\text{-value} < 0.05$) have brighter colour. Regions with a non-small relative future LAD change (>10% of

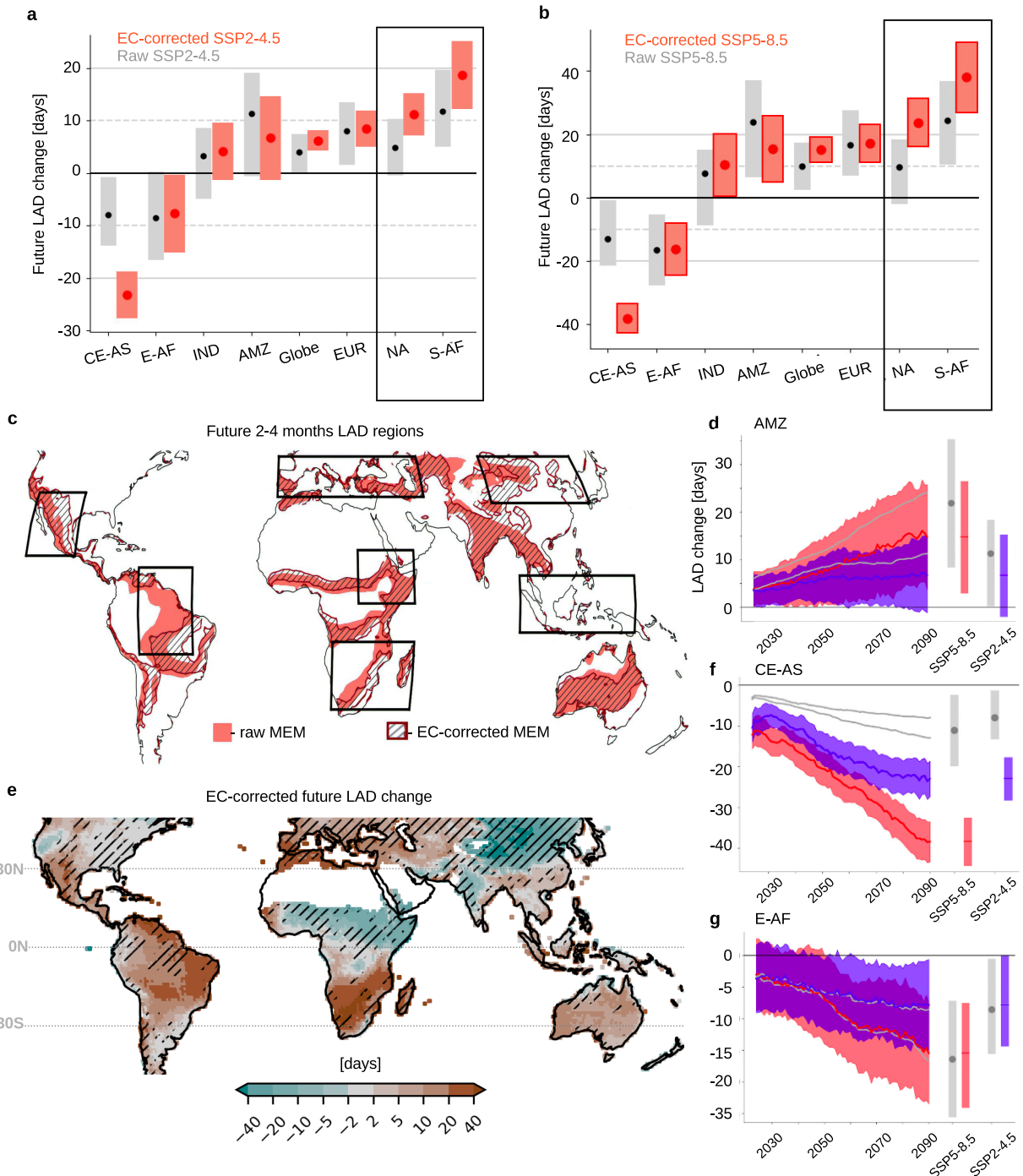
historical value) are hatched. **c**, Global statistics of correlations between historical LAD and future LAD change under SSP5-8.5 separated per p -value range are shown as box plots. Box plots show interquartile range (IQR, box) and 1.5 times IQR (whiskers) of data.

Article



Extended Data Fig. 7 | Sensitivity of EC-corrected future LAD change bias to observational spread. **a, b**, Future LAD change bias calculated using mean value of either three observational data sets with lowest global mean LAD, i.e. GPCP, TRMM-CMORPH, PERSIANN (see Methods) (**a**) or three observational data sets with highest global mean LAD, i.e. REGEN, GPCC, GSMAP (see Methods) (**b**) for EC correction. Masked in white are the regions with small

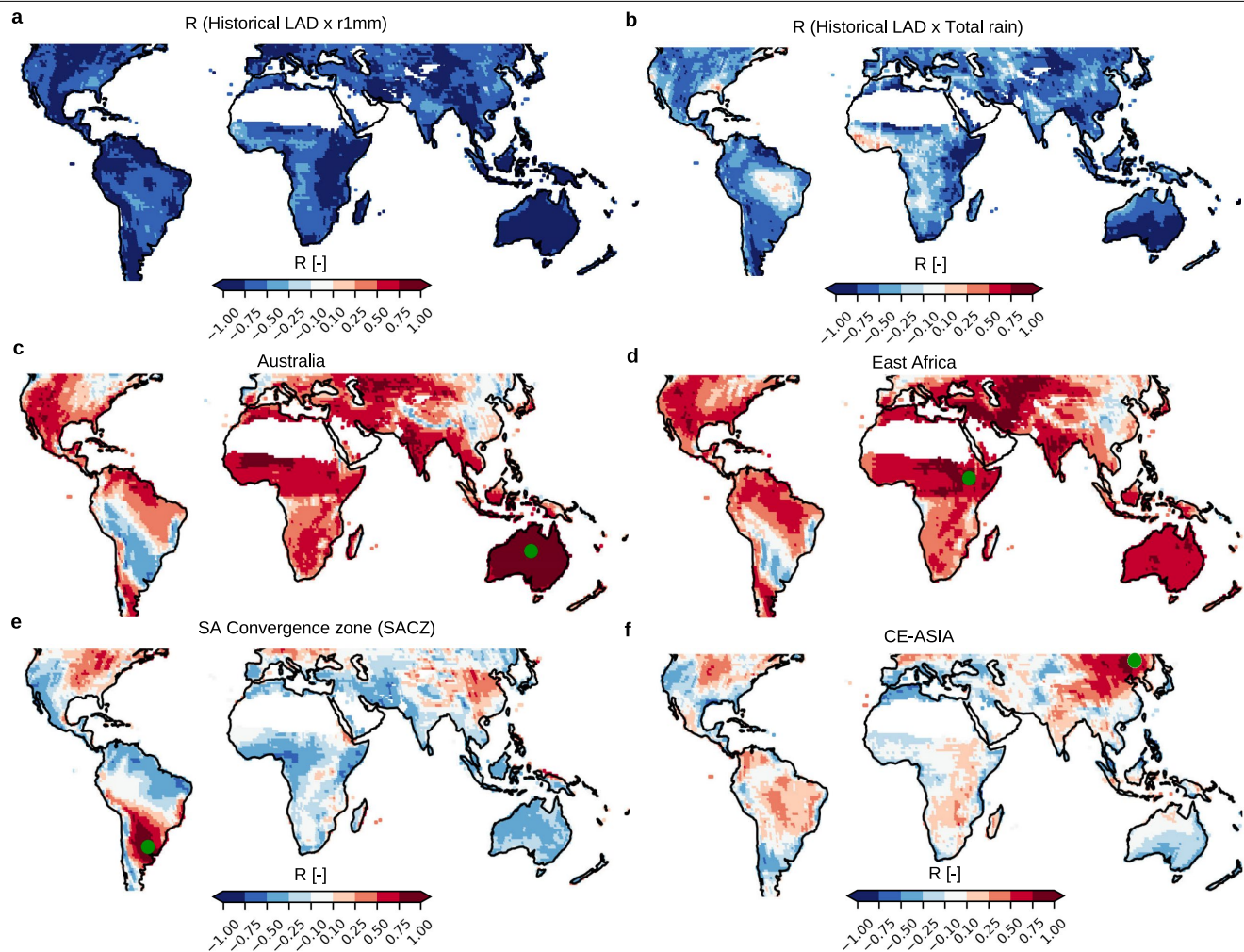
(<10%) 21st century relative change or regions with invalid LAD data (see Methods). Regions with a significant local EC correlation ($R > 0.4$ and $p\text{-value} < 0.05$) are hatched. Boxes show two regions where change in sign between two groups is observed. **c**, Difference in historical LAD climatological mean between two observational groups. **d**, Difference in EC-corrected future LAD change bias between both groups.



Extended Data Fig. 8 | Calibrated future LAD projections for CMIP6 models. **a,b** End-of-century raw and EC-corrected MEM LAD change averaged per hotspot region under **(a)** SSP2-4.5 and **(b)** SSP5-8.5 scenarios. Bar plots show the 66% of model ensemble values for raw (grey) and EC-corrected (red) LAD change projections. **c**, Spatial shift (before and after EC correction) in global areas of 2 to 4 month climatological LAD under the SSP5-8.5 scenario for the end of the century. **e**, EC-corrected future (SSP5-8.5) LAD climatology for

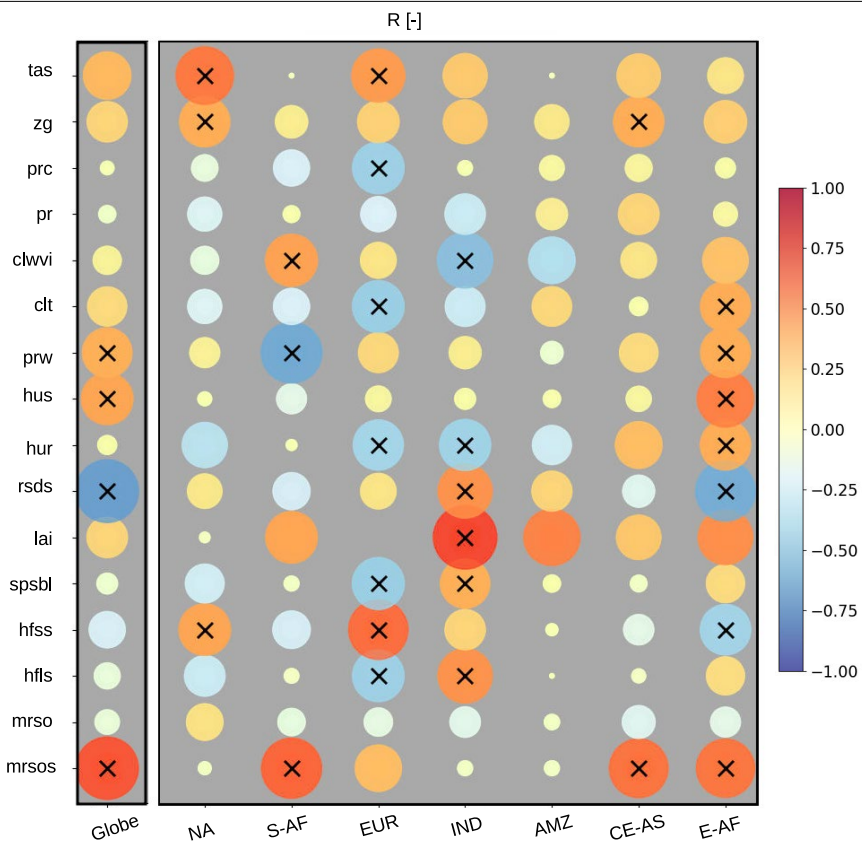
2080–2100. Hatched areas show regions with a significant local EC correlation ($R > 0.4$ and $p\text{-value} < 0.05$). **d,f,g**, Time-series of raw (grey) and EC-corrected (colour) annual projections of LAD change in three global hot-spot regions for two emission scenarios. Time-series are smoothed using 20-year running mean. Bars and time-series uncertainty ranges represent the 66% of model ensemble values for the end-of-century and annual statistics, respectively.

Article



Extended Data Fig. 9 | Local correlation of LAD to precipitation and global consistency in EC correlation. **a,b**, Pearson correlation between historical LAD and total annual number of **(a)** wet days (rain <1 mm/day), and **(b)** total annual precipitation. **c-f**, Inter-model correlation of historical CMIP6 LAD

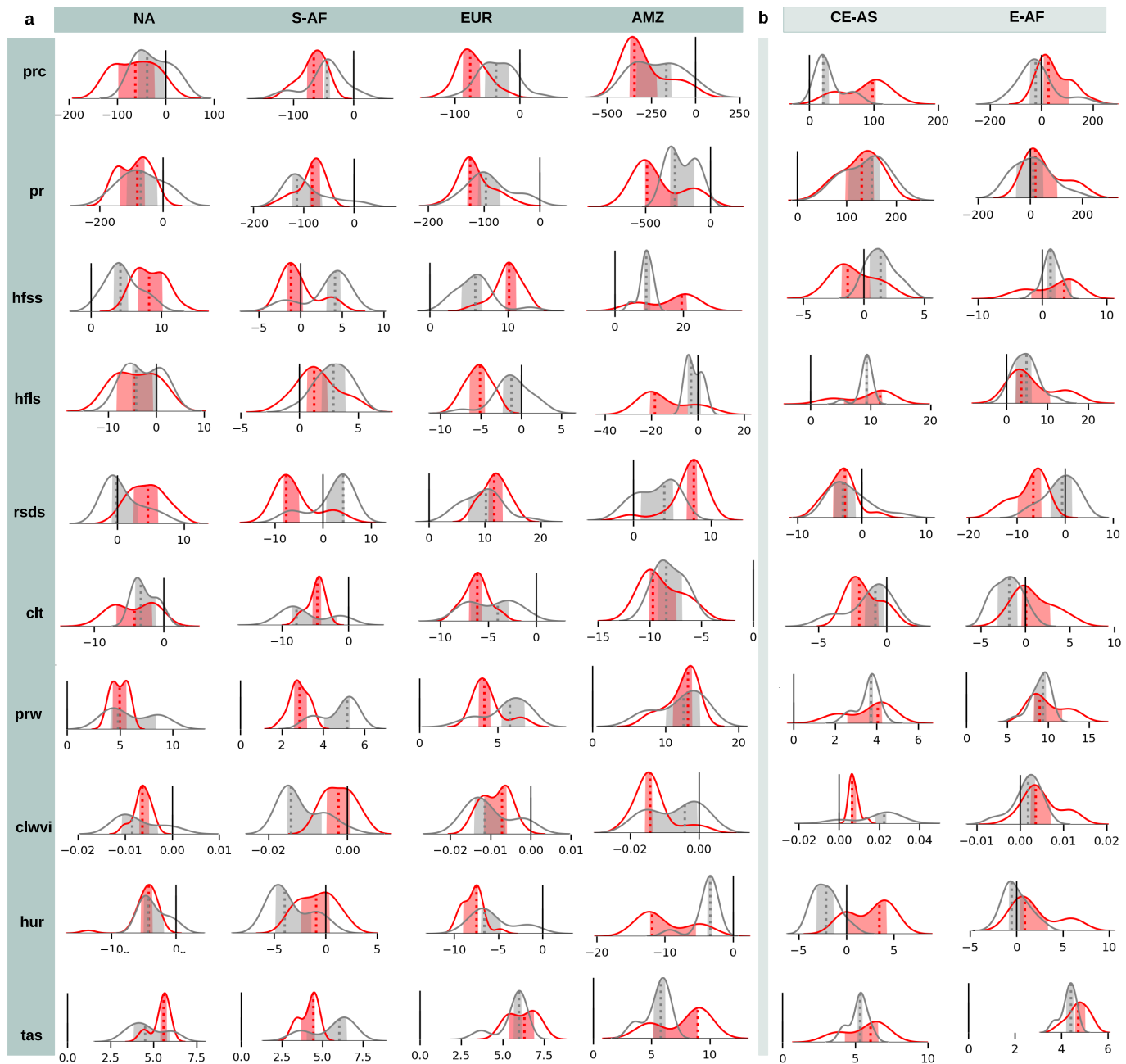
climatology in a pixel from **(c)** Australia, **(d)** East Africa, **(e)** South Atlantic Convergence Zone (SACZ), and **(f)** CE-Asia to the historical CMIP6 LAD scatter in rest of the world. Note, SACZ and CE-ASIA appear as locally correlated features decoupled from the rest of regions with high local EC correlation.



Extended Data Fig. 10 | Inter-model correlation of historical LAD to the corresponding future projected change in hydro-climatic variables. The value of Pearson correlation assessed for every domain separately is shown in

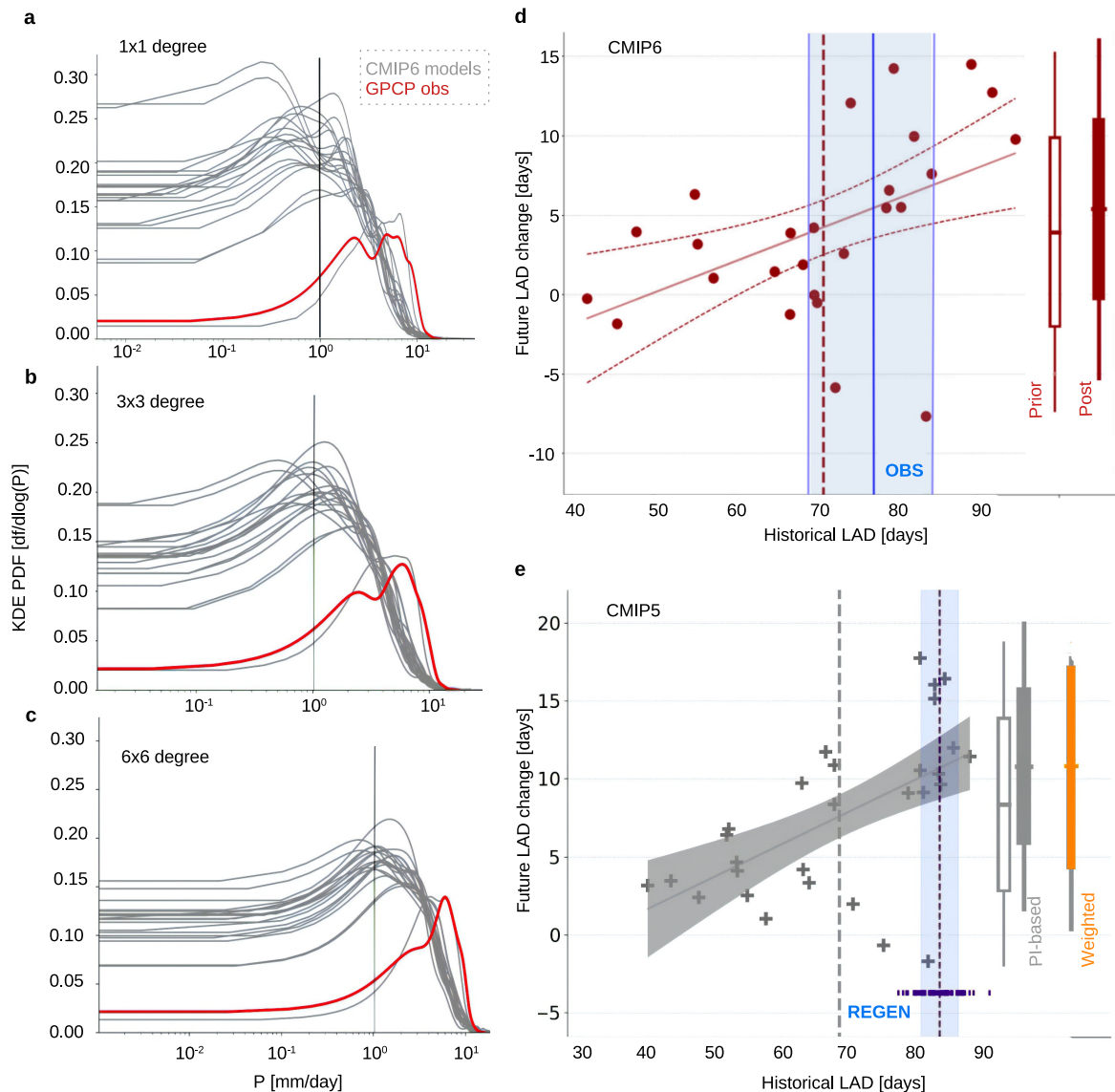
colour. Correlations significant at p -value < 0.01 level are marked with a cross. Names of variables are decoded in Table S4. Future changes for the variables are assessed during local dry periods (see Methods).

Article



Extended Data Fig. 11 | Differences in future projections of hydro-climatic variables between 'dry' and 'wet' models. **a,b**, KDE-based distribution frequencies of future projected changes in selected hydro-climatic variables in CMIP6 models (see Methods) following the SSP5-8.5 scenario for locally defined 'dry' (red) and 'wet' (grey) models in regions of future LAD **(a)** increase

and **(b)** decrease. Each distribution is built on model simulated data, which can include up to ten ensemble members, depending on their availability (see Methods). Shaded areas show the ± 1 standard deviation data range; dotted line shows the median value.



Extended Data Fig. 12 | Sensitivity of the EC relationship to the minimum daily rainfall threshold, model re-gridding procedure and future uncertainty estimation approach. **a–c**, KDE-based frequency distribution across global land (50°S – 50°N) daily rain rates in CMIP6 models (grey) and GPCP observations (red) (see Methods) over 1998–2014. Three panels represent sensitivity of results to data being upscaled to different grid resolutions. **d**, Global EC-relationship estimated for CMIP6 models at their original grid resolution. **e**, Globally averaged future LAD change projections before (empty bar), and after (filled bars) EC-correction using either PI-based approach as in Fig. 2 (gray filled bar) or K-L divergence approach²² (orange filled bar). 66 years

of REGENAIISat dataset (see Methods) and CMIP5 data of the same period are used to estimate the mean and variance of every model and observational data, and then to estimate weights to correct the future model projections using K-L divergence approach. In **d,e**, every dot/cross represents the global land average of a model. Corresponding MEM is shown as vertical dashed line. Blue shading shows the standard deviation of observed LAD climatology across observational data sets (**d**) and 66 years of REGENAIISat (**e**). Bars show the mean, 66 and 90% range of the future LAD prior (empty bar) and post (filled bar) EC correction.